2008

Large-scale structure of the molecular gas in Taurus revealed by high linear dynamic range spectral line mapping

PF Goldsmith

M Heyer

Gopal Narayanan
University of Massachusetts - Amherst

Ronald L. Snell
University of Massachusetts - Amherst

D Li

See next page for additional authors

Recommended Citation

Goldsmith, PF; Heyer, M; Narayanan, Gopal; Snell, Ronald L.; Li, D; and Brunt, C, "Large-scale structure of the molecular gas in Taurus revealed by high linear dynamic range spectral line mapping" (2008). *ASTROPHYSICAL JOURNAL*. 609.
10.1086/587166

Large–Scale Structure of the Molecular Gas in Taurus Revealed by High Linear Dynamic Range Spectral Line Mapping

Paul F. Goldsmith[1], Mark Heyer[2], Gopal Narayanan[2], Ronald Snell[2], Di Li[3], and Chris Brunt[4]

ABSTRACT

We report the results of a 100 square degree survey of the Taurus Molecular Cloud region in the J = 1 → 0 transition of ^{12}CO and of ^{13}CO. The image of the cloud in each velocity channel includes $\simeq 3\times10^6$ Nyquist-sampled pixels, sampled on a 20″ grid. The high sensitivity and large linear dynamic range of the maps in both isotopologues reveal a very complex, highly structured cloud morphology. There are large scale correlated structures evident in ^{13}CO emission having very fine dimensions, including filaments, cavities, and rings. The ^{12}CO emission shows a quite different structure, with particularly complex interfaces between regions of greater and smaller column density defining the boundaries of the largest–scale cloud structures. The axes of the striations seen in the ^{12}CO emission from relatively diffuse gas are aligned with the direction of the magnetic field. We have developed a statistical method for analyzing the pixels in which ^{12}CO but not ^{13}CO is detected, which allows us to determine the CO column in the diffuse portion of the cloud as well as in the denser regions in which we detect both isotopologues. Using a column density–dependent model for the CO fractional abundance, we derive the mass of the region mapped to be 2.4×10^4 $M_\odot$. This is more than a factor of two greater than would be obtained using a canonical fixed fractional abundance of ^{13}CO and a factor three greater than would be obtained using this fractional abundance restricted to the high column density regions. We determine that half the mass of the cloud is in regions having column density below 2.1×10^{21} cm^{-2}. The distribution of young stars in the region covered is highly nonuniform, with the probability of finding a star

[1]Jet Propulsion Laboratory, California Institute of Technology, 4800 Oak Grove Drive, Pasadena CA, Paul.F.Goldsmith@jpl.nasa.gov

[2]FCRAO, Department of Astronomy, University of Massachusetts, Amherst MA

[3]Jet Propulsion Laboratory, California Institute of Technology, 4800 Oak Grove Drive, Pasadena CA

[4]University of Exeter

in a pixel with a specified column density rising sharply for $N(H_2) = 6\times10^{21}$ cm^{-2}. We determine a relatively low star formation efficiency (mass of young stars/mass of molecular gas), between 0.3 and 1.2 percent, and an average star formation rate during the past 3 Myr of 8×10^{-5} stars yr^{-1}.

Subject headings: ISM: molecules – individual (carbon monoxide) ISM: structure; ISM:individual (Taurus)

1. INTRODUCTION

The close association of young stars and concentrations within molecular clouds indicates that stars form in cloud cores, which are regions of increased density within the bulk of molecular clouds (cf. Beichman et al. 1986). While the evolution from cloud core to protostar is dominated by gravity, the physics controlling the process in which the cores themselves, and the clouds in which they are embedded, are formed and evolve is still quite controversial. While on the scale of pc to tens of pc molecular clouds are close to satisfying virial equilibrium between gravitational and kinetic energies, the significance of this equality is not entirely clear. Furthermore, the role of magnetic field, while often postulated to be significant, remains uncertain (Shu et al. 1987; Heiles & Crutcher 2005). Finally, the formation of molecular clouds themselves, and their lifetime, remains very much a matter of discussion (e.g. Hartmann et al. 2001)

Molecular clouds may be formed by compression of atomic gas, with the increased density and extinction enhancing the formation rate of molecules, starting with H_2, for which self–shielding enables the buildup of a substantial fraction of the total hydrogen density even when the visual extinction A_V is only a fraction of a magnitude. It has also been suggested that the large molecular cloud presence in galactic spiral arms is the result of the agglomeration of molecular material existing in the interarm region, as discussed by Pringle, Allen, & Lubow (2001). While one viewpoint has held that molecular clouds have relatively long lifetimes, and are disrupted only by the energy injected by massive star formation and evolution, another picture is that molecular clouds are relatively transient objects, with the denser regions representing only turbulent fluctuations of density rather than well-defined gravitationally bound condensations (see e.g. review by Vázquez–Semadeni 2007).

These issues have been discussed on global scale, addressing the distribution of clouds and the apportioning of molecular and atomic gas in the Galaxy. They are also very relevant to studies of specific molecular cloud complexes, with one of the best–studied of these being that in Taurus. The structure of the interstellar gas in atomic and molecular form, the stellar

population, the issue of star formation rate, and the role of different physical processes have all been the subject of numerous papers focused on the Taurus region, primarily because its proximity (140 pc; Elias 1978)[1] allows very detailed studies of the morphology of the gas and the relationship between gas and stars. The sheer volume of the data that have been obtained and the number of analyses that have been carried out preclude giving a complete listing of the references to Taurus, so we will have to be selective rather than comprehensive, recognizing that we may have omitted many valuable contributions.

The very closeness of Taurus means that available instrumentation, particularly at radio frequencies, has faced a challenge to cover the entire region with angular resolution sufficient to reveal the morphology of the gas. The result has been that previous large–scale surveys of molecular line emission at millimeter wavelengths have been limited to quite low angular resolution (Ungerechts & Thaddeus 1987). The survey of Ungerechts & Thaddeus (1987) covers essentially all of Taurus and part of Perseus, but the $30'$ angular resolution of the map (obtained by averaging multiple telescope pointings to obtain a larger effective beam size) yields only 3000 pixels in the 750 square degree region mapped. The pixel size corresponds to a linear size of 1.2 pc at a distance of 140 pc, which is sufficiently large to blur out structure at important astrophysical scales. In fact, the maps of Ungerechts & Thaddeus (1987), while delineating the large–scale structure quite well, show an almost complete absence of fine detail. This is in part due to the use exclusively of ^{12}CO, which is sufficiently optically thick that significant variations in column densities can be entirely hidden, as well as to the low angular resolution.

There have been a number of investigations of molecular gas in the Taurus region with higher angular resolution, but these have typically been limited to small subregions within the overall gas distribution. These studies, with $\simeq 1'$ to $2'$ angular resolution include a few thousand to $\simeq$ 30,000 spatial pixels (Schloerb & Snell 1984; Duvert, Cernicharo, & Baudry 1986; Heyer et al. 1987; Mizuno et al. 1995). These studies, with the combination of higher angular resolution and use of the J = 1→0 transition of ^{13}CO do reveal considerable structure in the molecular gas, but have not elucidated its relationship to larger–scale features in the molecular gas distribution.

A number of other studies have utilized yet higher angular resolution and different tracers to probe gas having different characteristic properties over limited regions. Some examples include Langer et al. (1995) employing CCS, Onishi et al. (1996) and Onishi et al. (1998) using C^{18}O, Onishi et al. (2002) using H^{13}CO$^+$, and Tatematsu et al. (2004)

[1]This value, from Elias (1978), is so entrenched in the literature that we will use it despite the plausible suggestion by Hartigan & Kenyon (2003) that the distance should be reduced by about 10%, to ∼126 pc.

employing N_2H^+. Many individual cores have been observed in ammonia, a tracer in which they appear relatively well–defined, as indicated by compilation of Jijina, Myers, & Adams (1999). Most of the regions covered by these studies have been pre-selected based on the large–scale surveys discussed above. In these maps, we see indications of finer–scale structure, but the emission is generally quite spatially restricted compared to that seen in the more abundant isotopologues of carbon monoxide.

In this paper we present the initial results from a large–scale high angular resolution study of the Taurus molecular clouds using ^{12}CO and ^{13}CO. The data cover approximately 100 square degrees on the sky (11.5° in R.A. by 8.5° in decl.) corresponding to a region 28 pc by 21 pc. The reduced maps include 3.2×10^6 Nyquist–sampled pixels in each isotopologue, with pixel size 20″ corresponding to 0.014 pc. The linear dynamic range (LDR, defined as map size divided by Nyquist–sampled interval) of the maps thus exceeds 1000, which is the largest of any molecular cloud study carried out to date. The good angular resolution and large LDR together allow us to examine in detail the relationship between the relatively fine structures seen, especially in ^{13}CO, with the large–scale distribution of the molecular material, the young stars in the region, and the magnetic field.

The region of Taurus studied here has been observed using a variety of other tracers. The Leiden/Dwingeloo 21 cm study (Burton & Hartmann 1994) traced the atomic hydrogen in this direction, but with an angular resolution of 35′. One investigation (Shuter et al. 1987) used the Arecibo radio telescope having an angular resolution of 4′, but included only $\sim$ 1300 positions to probe the self–absorption seen in the 21 cm HI line. This cold atomic hydrogen appears to be associated with molecular gas (Li & Goldsmith 2003; Goldsmith & Li 2005), but the limited sampling of Shuter et al. does not reveal much about its morphology. The far–infrared emission from Taurus has been studied by Abergel et al. (1995), who also compared it to moderate resolution maps of ^{12}CO J = 1→0 emission. The dust column density distribution has been examined by Padoan et al. (2002) and does bear a quite close resemblance to the integrated intensity of ^{13}CO and thus to the column density of gas in relatively high extinction regions.

We discuss the observations and data reduction procedure in §2. Derivation of the column density in the different portions of the maps is presented in §3, in which we also discuss the distribution of column density and mass in the region. We present a brief discussion of the large–scale gas kinematics in §4. We address the relationship of the molecular material and the magnetic field in §5, and discuss the relationship of the gas and the young stars in the region in §6. We discuss some of the interesting features of the morphology of the gas in §7. We summarize our results in §8.

2. OBSERVATIONS

The observations were taken between 2003 November and 2005 May using the 13.7m radome–enclosed Quabbin millimeter wave telescope. The 32 pixel SEQUOIA focal plane array[2] receiver observed the J = 1→0 transition of ^{12}CO and ^{13}CO simultaneously. Since the receiver uses amplifiers for the first stage, there is no issue of the sideband gain uncertainty and its effect on calibration. Sixteen pixels are arranged in a 4 x 4 array in two orthogonal linear polarizations. The main beam of the antenna pattern had a full width to half maximum angular width of 45″ for ^{12}CO and 47″ for ^{13}CO.

The data were obtained using an on–the–fly (OTF) mapping technique. A standard position was observed using position switching several times per observing session to verify calibration consistency. Details of the data–taking, data reduction, and calibration procedures are given by Narayanan et al. (2007). The signals from a band of frequencies around each spectral line were sent to an autocorrelation spectrometer with 1024 lags covering 25 MHz for each spectral line. The lag spacing of the spectrometer system corresponds to 0.068 km s^{-1} for ^{13}CO and 0.065 km s^{-1} for ^{12}CO. The data cube of each isotopologue employed in the subsequent analysis included 76 spectral channels for ^{13}CO and 80 channels for ^{12}CO covering approximately -5 km s^{-1} to +14.9 km s^{-1} and thus included 2.4×10^8 voxels.

As discussed in detail by Narayanan et al. (2007), the overall quality of the data was excellent. After calibration and combination of the 30′ by 30′ submaps which were the units in which the data was taken, the data were resampled onto a uniform grid of 20″ spacing, which is very close to the Nyquist sampling interval $\lambda/2D$ for the 13.7 m diameter telescope operating at a wavelength of 2.6 mm. The images produced by the combination of the submaps and regridding were 2069 pixels in RA by 1529 pixels in decl., thus comprising 3,163,501 spatial pixels resampled onto a uniform 20″ grid. The final data set has a well–behaved distribution of noise with a mean rms antenna temperature equal to 0.125 K for ^{13}CO and 0.28 K for ^{12}CO in channel widths of 0.27 km s^{-1} and 0.26 km s^{-1}, respectively.

We show the basic ^{13}CO data in Figure 1, which gives the intensity of the ^{13}CO J = 1→0 transition integrated over the velocity range 2 km s^{-1} to 9 km s^{-1}. This interval encompasses almost all of the emission in the Taurus region, with the exception of some isolated areas with gas at $\simeq$ 10 km s^{-1}, which may well not be associated with Taurus, and a limited amount of emission in the velocity range 1 km s^{-1} to 2 km s^{-1}. Figure 2 displays the ^{12}CO J = 1→0 peak emission within this same velocity interval. Note that in both of these figures, the emission is not corrected for the antenna efficiency. Narayanan et al. (2007) present

[2]A 16 pixel single–polarization version of the array is described in Erickson et al. (1999).

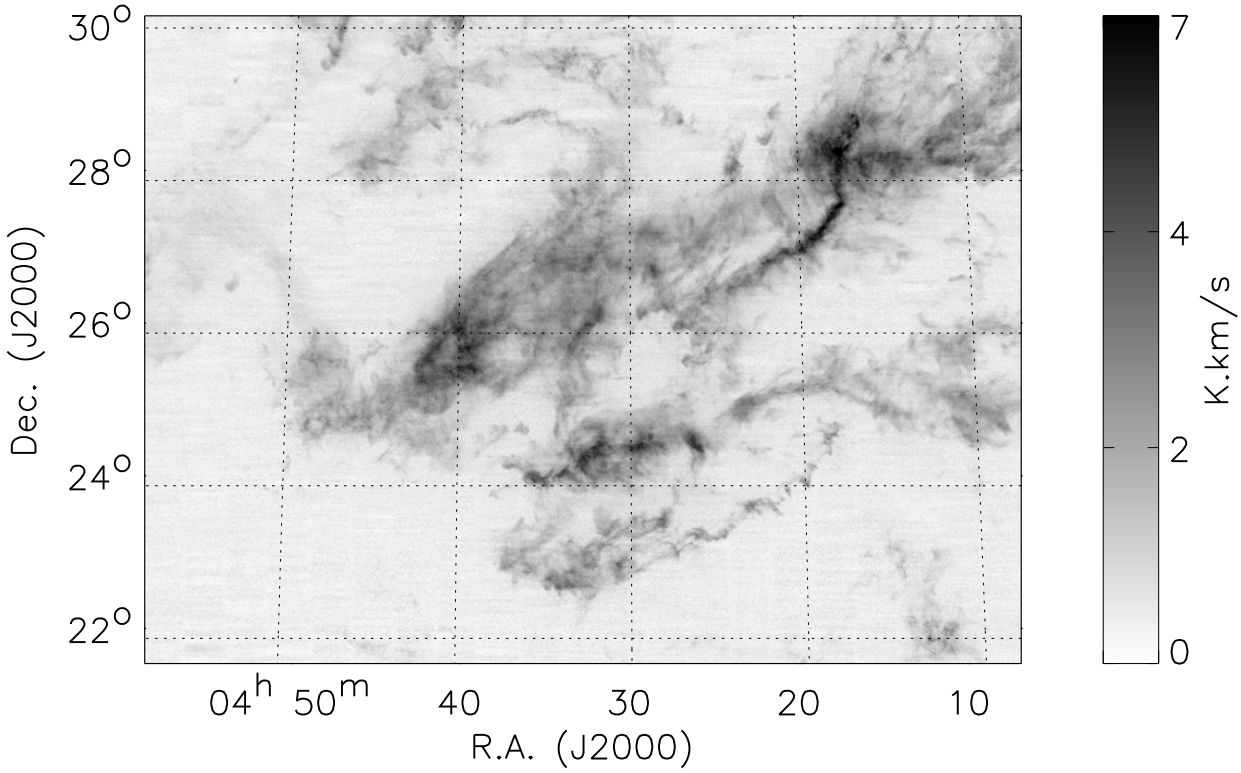

Fig. 1.— Antenna temperature of the ^{13}CO J = 1→0 transition integrated over the velocity range 2 km s^{-1} to 9 km s^{-1}. The scale is shown in the bar at the right; values have not been corrected for antenna efficiency.

images of the emission of both isotopologues in 1 km s^{-1} bins covering the range 0 km s^{-1} to 13 km s^{-1}.

It is evident that the ^{12}CO is detectable over a significantly larger area than is the ^{13}CO. Particularly in the northeast portion of the map, we see very extended ^{12}CO emission, where there is relatively little ^{13}CO. There are also two interesting regions of quite strong ^{12}CO emission, at 4^h22^m+28°30′ and 4^h48^m+29°40′, which are among the warmest regions observed, and yet which do not show up as significant local maxima in the ^{13}CO (and hence column density). In general, the warmer gas as traced by ^{12}CO is seen in regions of high column density, but the amount of structure seen in the optically thick ^{12}CO with our angular resolution, sampling, and sensitivity, is very impressive.

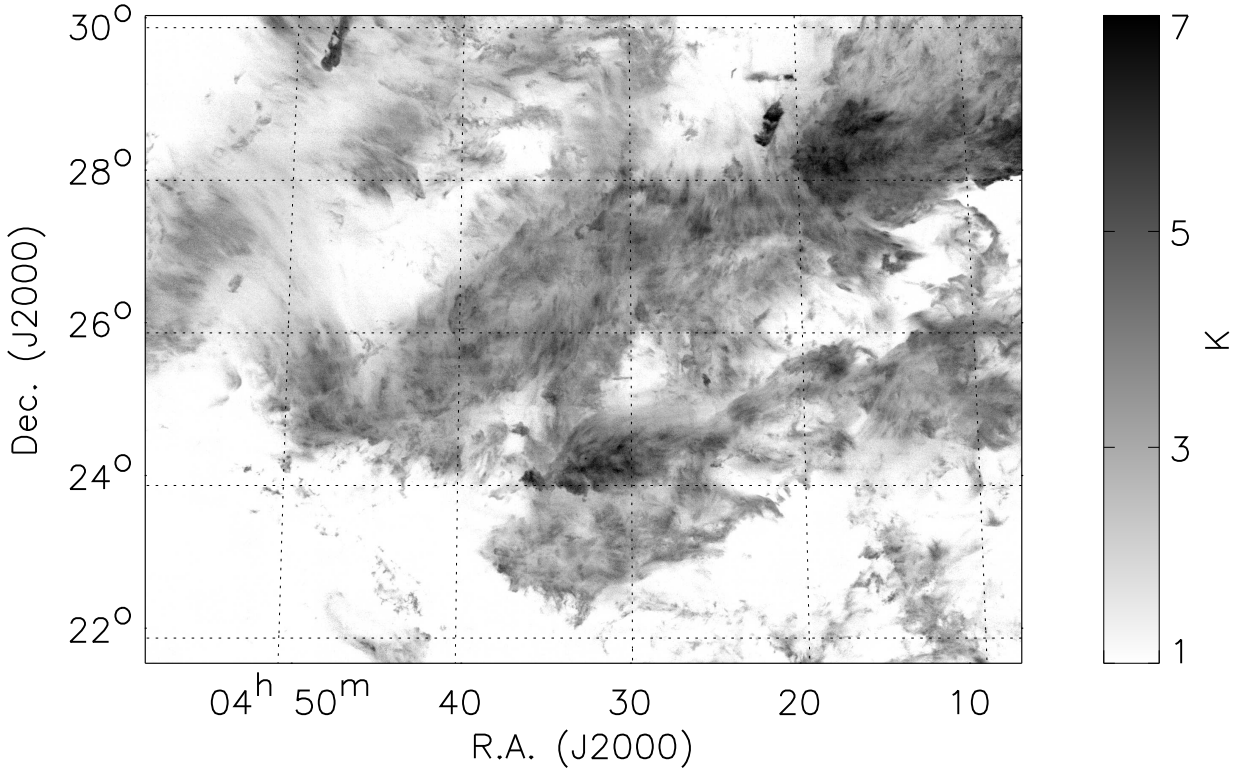

Fig. 2.— Maximum antenna temperature of the ^{12}CO J = 1→0 transition over the velocity range 2 km s^{-1} to 9 km s^{-1}. The antenna temperature has not been corrected for the antenna efficiency.

3. COLUMN DENSITY, COLUMN DENSITY DISTRIBUTIONS, AND CLOUD MASS

3.1. Mask Regions

In order to facilitate analysis of the data to determine column densities, we have broken the Taurus data up into 4 regions, according to the detection or nondetection of ^{12}CO and ^{13}CO. The detection thresholds are defined by the requirement that the integrated intensity over the velocity range extending from 0 km s^{-1} to 12 km s^{-1} be a minimum of 3.5 times larger than the rms noise in an individual pixel over this 12 km s^{-1} velocity interval. The median values are $\sigma_{T_{int}} = 0.18$ K kms^{-1} for ^{13}CO and $\sigma_{T_{int}} = 0.40$ K kms^{-1} for ^{12}CO. Since the peak values of the integrated intensity are 6 K kms^{-1} for ^{13}CO and 18 K kms^{-1} for ^{12}CO, the peak integrated intensities are 30 to 50 $\sigma_{T_{int}}$.

We define mask 0 to be the region in which neither ^{12}CO nor ^{13}CO is detected, mask 1 to be the region in which ^{12}CO is detected but ^{13}CO is not, mask 2 to be the region in which both isotopologues are detected, and mask 3 to be the region in which ^{13}CO is detected but ^{12}CO is not. The different regions and the number of pixels in each are given in Table 1.

The average spectra of mask 0, mask 1, and mask 2 regions are shown in Figure 3. These profiles are valuable for deducing general characteristics of the regions, but it must be kept in mind that the characteristics of the average profile are quite different from those of individual profiles. The difference is primarily due to systematic velocity shifts across the cloud; these result in the average spectra being much weaker and broader than individual spectra. The line width of the averaged mask 1 spectra is close to a factor of 2 greater than the average line width of spectra in this region. For mask 2, the ratio is $\simeq$1.5. Along with this, the peak intensities are much weaker than those seen in individual spectra or even in spectra averaged over a restricted region. Consequently, in determining characteristics

Table 1. Mask Regions in the Taurus Map

Mask Region	Characteristics	Number of Pixels
0	neither ^{12}CO nor ^{13}CO	944,802
1	^{12}CO but not ^{13}CO	1,212,271
2	both ^{12}CO and ^{13}CO	1,002,955
3	^{13}CO but not ^{12}CO	3,473

of the molecular gas, we have used individual spectra wherever possible to derive physical quantities.

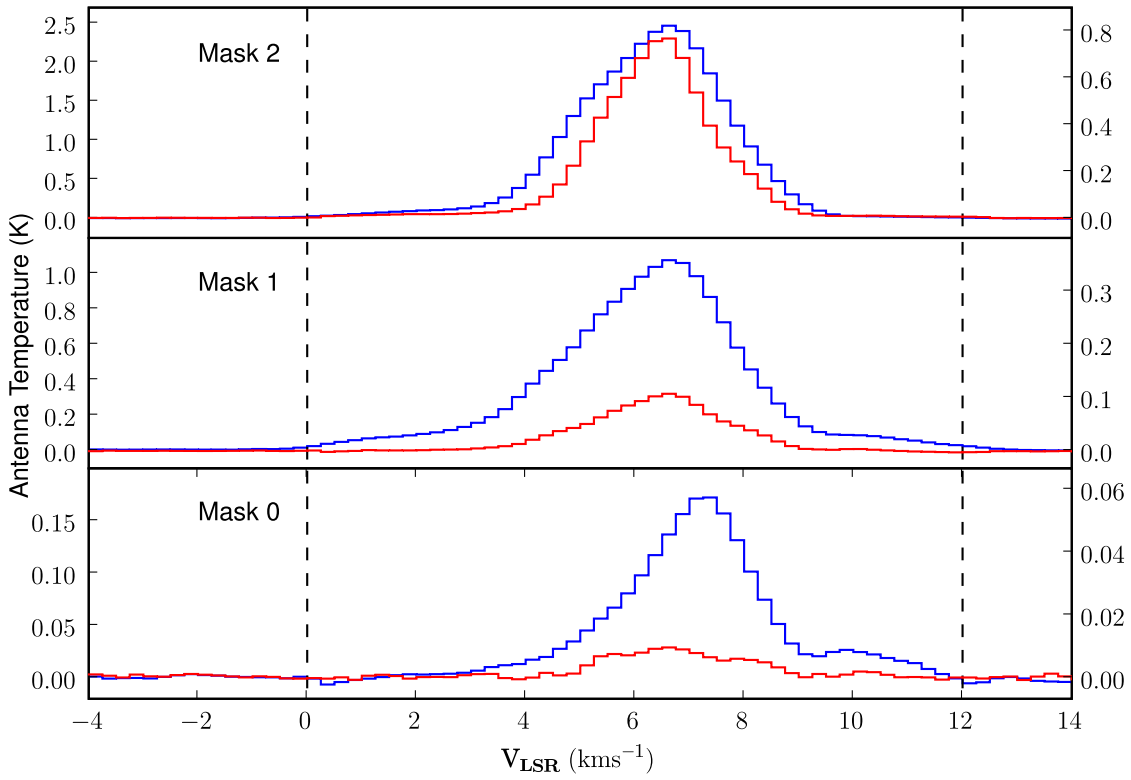

Fig. 3.— Spectra averaged in each of the three significant mask regions of the Taurus map, arranged from mask 0 (bottom) to mask 2 (top). In each panel, the ^{12}CO J= 1→0 spectrum is the more intense (blue), while the weaker ^{13}CO spectrum is plotted in red. The antenna temperature scale for the ^{12}CO is on the left hand side, while that for the ^{13}CO is on the right hand side, expanded by a factor of three relative to that of ^{13}CO. The dashed vertical lines delineate the velocity range used to define the material in the Taurus region.

As expected, the lines are strongest in mask 2. The ^{12}CO to ^{13}CO ratio at the line peak in mask 2 is just over 3, consistent with relatively high optical depth in the more abundant isotopologue. We do see that when an average over $\sim 10^6$ pixels of mask 1 is formed, we readily see emission in ^{13}CO as well as ^{12}CO. The ratio of peak intensities is significantly larger in mask 1 than in mask 2. The value, about 10, is still much less than the presumed abundance ratio [^{12}CO]/[^{13}CO], suggesting that the ^{12}CO in mask 1, while optically thick, typically has lower opacity than in mask 2.

The mask 0 ^{12}CO and ^{13}CO spectra show two or three peaks, including velocities for which the emission in mask 2 is very weak compared to that in the range of the peak emission, 5 km s^{-1} to 8 km s^{-1}. In particular, the 10 km s^{-1} emission feature comes from a fairly extended region in the northern portion of our map, but is so weak that only when averaging over modest-sized ($\sim$1 square degree) regions in mask 0 can it be detected. Emission in this velocity range can be quite clearly seen in the mask 1 spectrum, but hardly can be detected in mask 2. This is consistent with it being relatively low average column density material, which is extended over quite large areas. Thus, even in what we consider largely "empty" regions between the major, well–known subunits of the Taurus molecular cloud complex, there is molecular gas. This is discussed further in the following section. The overall composition of the mask 0 region, particularly the presence of atomic gas, is the subject of another study.

The mask 0, mask 1, and mask 2 regions have close to equal numbers of pixels. Their distribution, however, is very different. Figure 4 shows the four mask regions. It is evident that the mask 1 predominantly surrounds mask 2, which is consistent with the expectation that both isotopologues are detected in the regions of highest column density (mask 2) while in the periphery of these regions we detect in individual pixels the ^{12}CO but not the ^{13}CO emission.

The pixels in mask 3 are unusual inasmuch as they exhibit detectable ^{13}CO emission but not ^{12}CO. There are evidently very few such pixels ($\simeq$ 0.1% of the total), although this number is considerably larger than would be expected purely on the basis of Gaussian noise statistics. On close inspection of these spectra, it appears that the problem is due to very low level baseline imperfections partially canceling the ^{12}CO integrated intensity, resulting in a "non–detection" of this isotopologue. We thus ignore the mask 3 pixels in further analysis of the emission from Taurus.

3.2. Calculation of the Column Density

We wish to exploit the large linear dynamic range of our map to examine the structure in the column density, and thus wish to determine the column density for as many pixels as possible. This is also important for accurately determining the total molecular mass of the region. In what follows we divide the problem into two parts. The first is determination of the carbon monoxide column density. While subject to its own uncertainties due to excitation, optical depth, and limited signal to noise ratio, we can carry out this step of the analysis based only on data in hand. The second step is conversion of the carbon monoxide column densities to molecular hydrogen column densities, and finally to total cloud mass. This is evidently dependent on the processes which determine the fractional abundance of

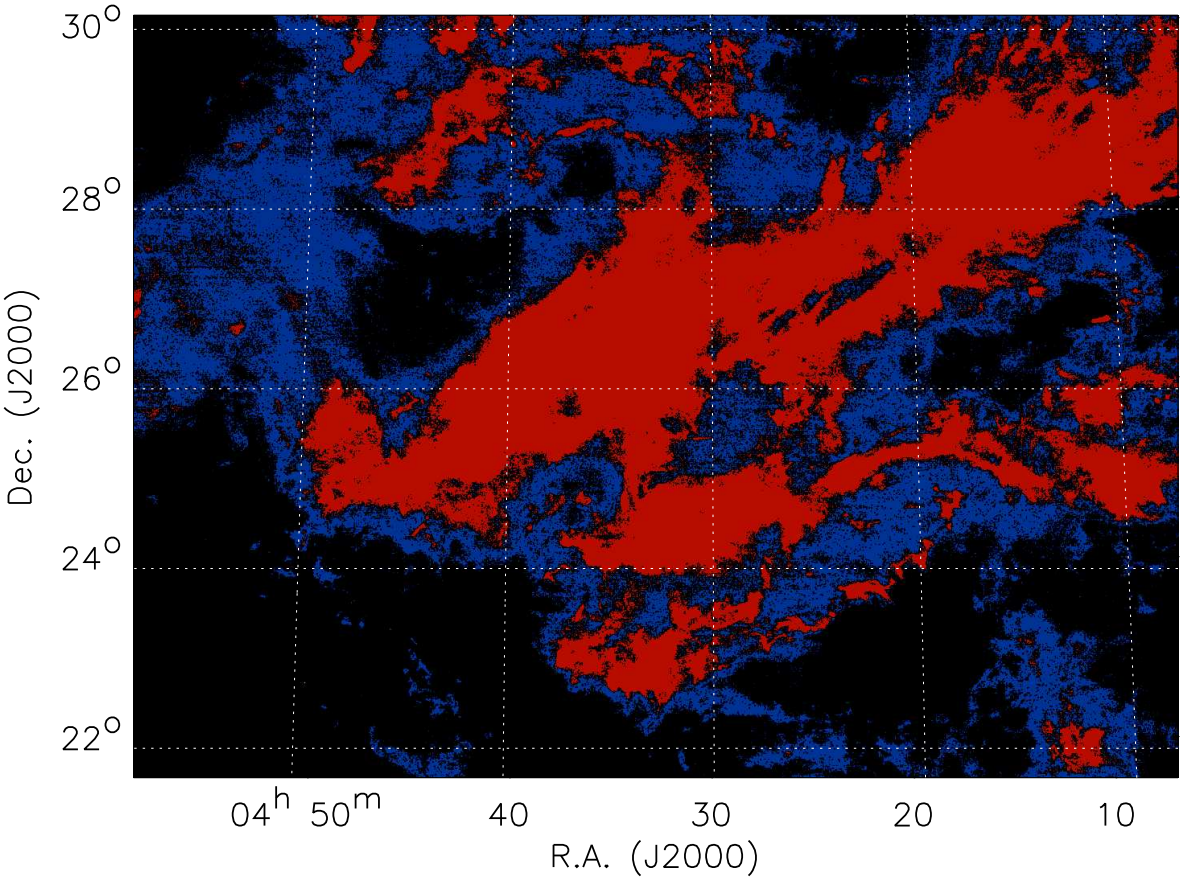

Fig. 4.— Image showing the mask regions (see text for definitions) in the Taurus molecular cloud. Mask 0 is shown in black, mask 1 in blue, and mask 2 in red. The relatively few mask 3 pixels are not shown.

the various isotopologues observed. Since the additional uncertainties in the second step are large, we present results first in terms of the carbon monoxide distribution and subsequently give results for the molecular hydrogen distribution and the total molecular mass. This second step should benefit significantly from combination of our data with dust column density determined from e.g. 2MASS data. This effort is in progress and will be reported in a subsequent publication.

3.2.1. Carbon Monoxide Column Density

The three different different regions of the cloud, defined by the detectability of each isotopologue, require different schemes to determine the carbon monoxide column density. We ignore mask 3 in determining the column density and to the mass of the cloud as we cannot readily correct for the artificial non–detections of ^{12}CO (discussed above). Its extremely small area and weak ^{13}CO emission make its contribution negligible.

Mask 2 represents the portion of the cloud that is most conventional in terms of column density determination. Since we have both ^{12}CO and ^{13}CO in each pixel, we determine the kinetic temperature from the peak value of the ^{12}CO (with appropriate correction for antenna efficiency). Here (as well as for other mask regions), we use the maximum antenna temperature of ^{12}CO in the velocity interval between 0 km s^{-1} and 12 km s^{-1}. The kinetic temperature is distributed from 3 K to 21 K, but with the vast majority of positions having kinetic temperatures between 6 K and 12 K. Since mask 2 is the densest portion of the cloud, we assume that the ^{13}CO levels are populated in LTE at the kinetic temperature, but we calculate a nominal value for the optical depth from the ratio of the peak ^{13}CO and ^{12}CO intensities using the usual equation of radiative transfer in a uniform medium. We assume a ^{12}CO to ^{13}CO abundance ratio of 65, very close to the average value for local clouds found by Langer & Penzias (1993). We use the value of optical depth obtained to make a saturation correction to the ^{13}CO column density derived assuming optically thin emission, with the usual formula

$$N(^{13}\mathrm{CO\ corrected}) = \mathrm{N}(^{13}\mathrm{CO\ assumed\ optically\ thin})\frac{\tau}{1-\exp(-\tau)}\ . \qquad (1)$$

Mask 1 presents the greatest challenge in terms of column density determination since it encompasses approximately one third of the area mapped and has reasonably strong ^{12}CO emission. However, since the ^{13}CO is not detected in individual pixels, we need a different scheme to extract the column density. We have developed a statistical approach, which should be applicable to other large maps in which only the more abundant isotopologue is detected in individual pixels. The procedure assumes that the ^{12}CO is optically thick at

its peak, and that the value of the antenna temperature can directly be converted to the excitation temperature of the ^{12}CO. Since mask 1 points lie at the periphery of the regions of high extinction and greater molecular column density (as witnessed by the detection of ^{13}CO in each mask 2 pixel), they encompass lower column density gas which is presumably characterized by lower volume density. Therefore we cannot assume that LTE applies as it does in mask 2. Approximately half of the mask 1 positions have an excitation temperature $\leq$ 7.5 K, and if in LTE the gas would have to be unusually cold. It is thus reasonable to assume that this gas is subthermally excited. To analyze positions in mask 1 we use a simple excitation/radiative transfer analysis employing a spherical cloud large velocity gradient (LVG) code to compute the line intensities (e.g. Snell 1981; Goldsmith, Young, & Langer 1983). We are using an LVG model largely as a tool to characterize the effect of trapping, which is important for excitation of CO at lower density. We do not believe it necessarily represents any statement about the detailed kinematics of the gas. The sensitivity of our results to the details of the velocity field should be quite small.

We have assumed that the kinetic temperature of the mask 1 region is uniformly 15 K, somewhat higher than well-shielded dense gas, which is plausible in view of increased heating in the peripheral regions surrounding regions of high extinction. (e.g. Li, Goldsmith, & Menten 2003). We take advantage of the large number of pixels in our map, and bin the data according to the excitation temperature of the ^{12}CO determined as described above. In each bin, we have a sufficient number of pixels that the ^{13}CO J = 1$\rightarrow$0 line is detected with good signal to noise ratio. For each T_{ex} bin, we then have the ^{12}CO excitation temperature and the observed ^{12}CO/^{13}CO integrated intensity ratio. The data generally have the observed intensity ratio decreasing with increasing T_{ex}, from $\simeq$ 22 for T_{ex} = 4.5 K to $\simeq$ 13 for T_{ex} = 2.5 K. The free parameters are the ^{12}CO column density, the H_2 density, and the ^{12}CO/^{13}CO abundance ratio. The latter cannot be assumed to be a fixed value (e.g. 65), due to the complicating presence of isotopic enhancement due to chemical and/or photo effects (e.g. Watson et al. 1976; Bally & Langer 1982; Chu & Watson 1983; Van Dishoeck & Black 1988). We thus consider R = ^{12}CO/^{13}CO between 25 and 65.

With three free parameters and only two observables, we cannot uniquely determine the properties of the gas in mask 1. Rather, we compute for each T_{ex} bin, a family of R, density and CO column density per unit line width solutions. If we knew *a priori* the value of R, then we could compute a unique density and CO column density per unit line width for each T_{ex}. With no knowledge of R, then the values of density and CO column density per unit line width span a range of approximately a factor of 4, with density and CO column density per unit line width inversely correlated. The family of solutions for the physical parameters of the gas show some significant general characteristics. First, for higher values of T_{ex}, only solutions with $R \geq 50$ fit the data. This is encouraging as the higher excitation

gas has on average the largest column density and we do not expect significant fractionation in the more shielded regions. On the other hand, for lower values of T_{ex}, values of R as large as 65 are excluded, and the range of acceptable solutions gradually shifts from $R \leq 50$ at $T_{ex} = 7.5$ K to values of $R \leq 30$ at $T_{ex} = 4.5$ K. Correspondingly, the allowable solutions for the gas density and CO column density per unit line width decrease with decreasing excitation temperature. This trend again is consistent with increasing fractionation in the less well–shielded regions at the periphery of the clouds (see Liszt 2007) for a discussion of this effect in diffuse clouds). These regions dominate the positions found within our mask 1. This result agrees with the behavior found in previous observational studies (e.g. Goldsmith et al. 1980; Langer et al. 1980; Young et al. 1982; Langer et al. 1989; Goldsmith & Li 2005; Kainulainen et al. 2006).

It is not possible to model the mask 1 observations with a fixed value of the *in situ* carbon monoxide isotopic ratio but rather require that the value of R vary significantly with excitation temperature. We have chosen solutions such that R varies smoothly from a value of 65 at $T_{ex} \geq 12.5$ K to a value of 30 for $T_{ex} = 4.5$ K. With this choice of R, we find that the gas density and CO column density per unit line width both increase monotonically with increasing excitation temperature. The solutions we have chosen are shown in Table 2 and in Figure 5. We emphasize that these solutions are not unique, but depend on our choice of R. However, the general behavior of the solutions are physically plausible, given that we expect the excitation temperature to increase as one moves from the cloud interior to the cloud periphery. This suggests that binning by T_{ex} is a useful approach, and gives us a reasonable handle on how the physical conditions vary as a function of excitation temperature and position in the cloud.

Our assumption of 15 K for the kinetic temperature is a potential source of error in determining the carbon monoxide column density. To assess this, we have carried out some calculations using a kinetic temperature of 25 K which seems an upper limit to what one might expect in a cloud edge in a region with modest UV intensity. We find that for this value of the kinetic temperature, the column density per unit velocity gradient is approximately a factor 1.5 larger than for a kinetic temperature of 15 K, and the derived H_2 density is a factor of 2.5 lower, for an assumed value of R. The same trends of carbon monoxide column density and H_2 density as a function of R are seen for the higher kinetic temperature as for the lower. The uncertainty resulting from the assumption of a fixed kinetic temperature is thus of the same order as resulting from our choosing a best value of R, and combining these could yield a factor of 2 uncertainty in $N(\mathrm{CO})$. Observations of multiple transitions of carbon monoxide isotopologues would provide a more accurate estimate of the molecular column density. However, observations of these transitions over a region of comparable size would pose a formidable challenge for currently available telescopes and receiver systems.

To obtain the column density for each line of sight, we utilize an analytic fit to the relationship between the CO column density per unit line width and the excitation temperature obtained for the set of T_{ex} bins, $N(^{12}CO)/\delta v = (-1.473 \times 10^{16} + 4.672 \times 10^{15} T_{ex})$. We multiply the results by the observed FWHM ^{12}CO line width Δv from the data. The use of the LVG model introduces some uncertainty because the carbon monoxide excitation is quite subthermal, and the excitation temperature does depend on the optical depth, and is quite different for ^{12}CO and ^{13}CO. Nevertheless, the likely error in the trapping predicted by the LVG and other models is relatively modest compared to other uncertainties inherent in this analysis.

In mask 0, after averaging $\simeq 10^6$ spatial pixels, we are able to detect both isotopologues, and we thus analyze the emission for the region as if it were a single spatial entity. The general analysis follows the procedure described above for mask 1. The fact that the integrated ^{12}CO/^{13}CO ratio is $\simeq 19$ indicates that the ^{13}CO is almost certainly optically thin. This is also the case for mask 1, and here as well results in the ^{12}CO and ^{13}CO having quite different excitation temperatures due to the radiative trapping for the more abundant isotopologue.

Again, we fix the kinetic temperature to be 15 K, reflecting increased heating in regions of low extinction, and assume that the average line width is 2 km s^{-1}, similar to that observed for the low excitation gas of mask 1. Note that the average mask 0 spectrum (Figure 3) is much broader than 2 km s^{-1}, but the large value of the line width reflects changes in the line center velocity over the entire region observed. Following the trend of R from mask 1, we assume this ratio to have a value of 20.

The mask 0 data cannot be fit satisfactorily by larger values of R thus confirming that relatively strong isotopic selective effects are at work in the low density/low column density regions of Taurus. With these assumptions, the parameters we derive, although again not unique as described above, are $n(H_2) = 75$ cm^{-3}, and $N(^{12}\mathrm{CO}) = 7.5{\times}10^{15}$ cm^{-2}. The carbon monoxide excitation in this region is evidently highly subthermal, consistent with the low derived H_2 density and the modest ^{12}CO optical depth. This very low value for the density of the mask 0 region gives a reasonably low column density for the extended component of the gas in Taurus. Taking a representative dimension for mask 0 of $1.5{\times}10^{19}$ cm^{-2}, we obtain $N(H_2) = 1.1{\times}10^{21}$ cm^{-2}. This corresponds to $A_v \simeq 1$ for the extended component of the cloud, consistent with that determined from stellar reddening (Cernicharo & Guélin 1987).

The spatial distribution of column densities from the three mask regions is shown in Figure 6. The column density for mask 0 is a single value $< N(^{12}CO) > = 7.5{\times}10^{15}$ cm^{-2} as given above. The column density distribution in the mask 1 region is a relatively symmetric, fairly Gaussian distribution with a mean value $< N(^{12}CO) > = 3.6{\times}10^{16}$ cm^{-2}. The column

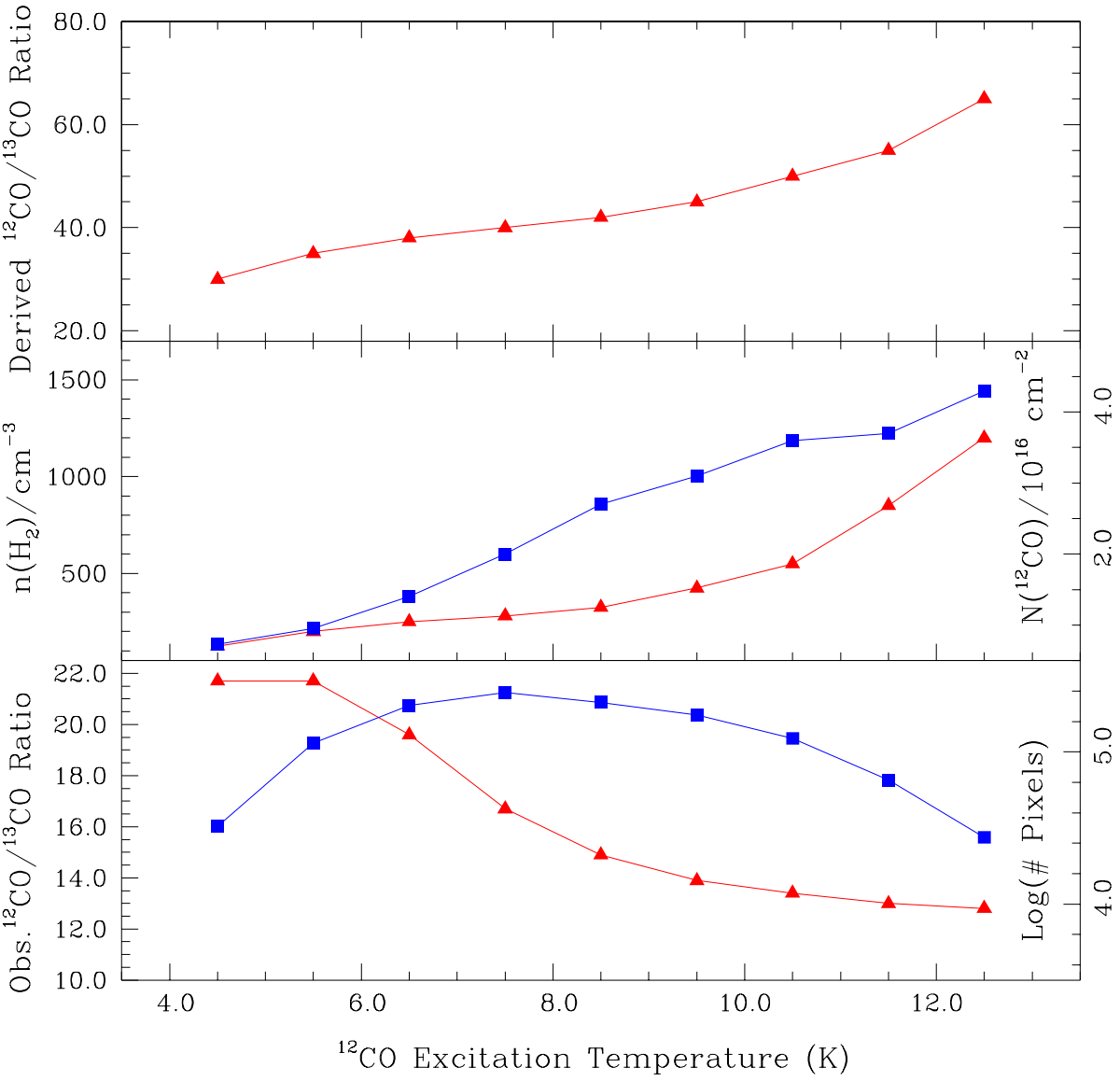

Fig. 5.— Parameters of mask 1 pixels binned by ^{12}CO excitation temperature T_{ex}. The bottom panel shows the observed ^{12}CO/^{13}CO intensity ratio (left hand scale; triangles), and the number of pixels in each excitation temperature bin (right hand scale; squares). The most common excitation temperatures are between 6 K and 10 K. The middle panel shows the H_2 density (left hand scale; triangles) and ^{12}CO column density assuming a line width of 1 km s^{-1} (right hand scale; squares). These are obtained from the ^{12}CO and ^{13}CO intensities. The top panel shows the derived ^{12}CO/^{13}CO abundance ratio. The H_2 density, ^{13}CO column density, and the derived ^{12}CO^{13}CO ratio all increase monotonically as a function of ^{12}CO excitation temperature.

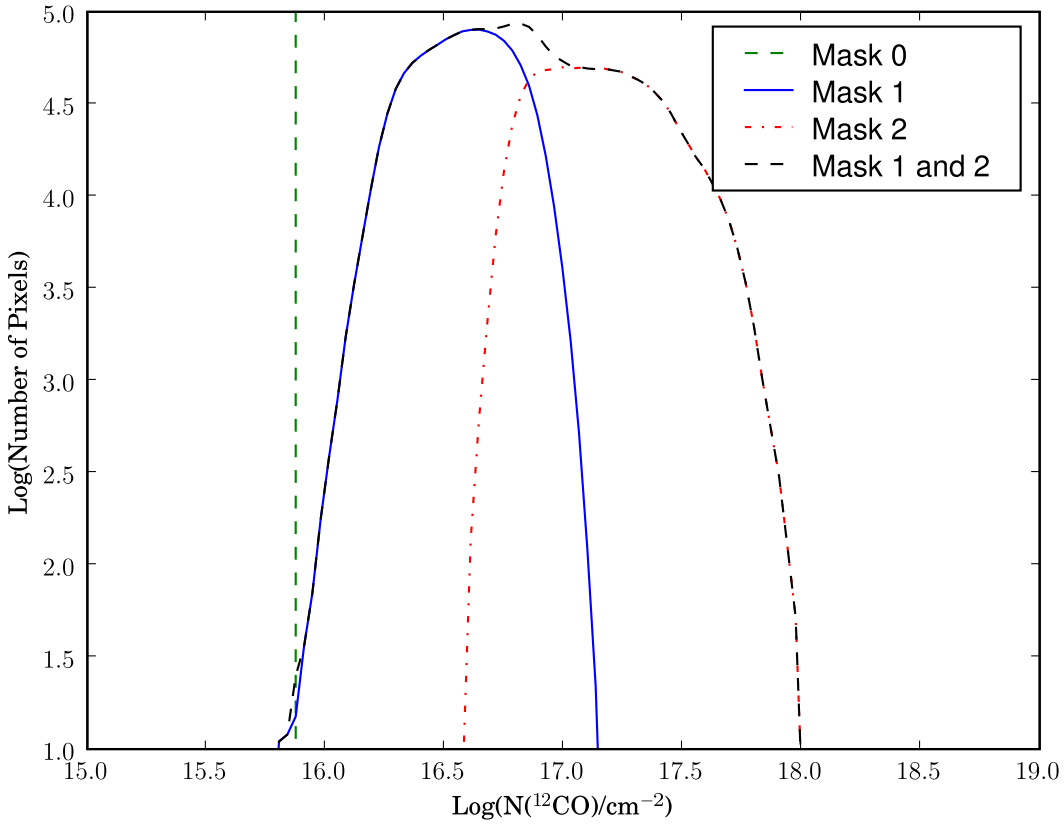

Fig. 6.— Histogram of ^{12}CO column density distributions in mask 0, 1, and 2 regions mapped in Taurus. The mask 0 data are indicated by the vertical dashed line, which represents the approximately 10^6 pixels in this region. The distribution for mask 1 is shown by the solid (blue) curve, that for mask 2 by dot–dashed (red) curve, and the combination of the two regions by the long–dashed (black) curve. The abscissa is the logarithm of the ^{12}CO column density, defined in bins of width 0.1 dex, except for mask 0 which is a single value. The ordinate is the logarithm of the number of pixels in each column density bin. The total number of pixels included is close to 3.1 million.

density distribution in the mask 2 region is flat–topped with a mean value $< N(^{12}CO) > = 1.3{\times}10^{17}$ cm^{-2}.

The distribution of carbon monoxide in the Taurus region is shown in Figure 7. This figure dramatically illustrates the complexity of the molecular gas distribution. The impression given is quite different from that of studies with low angular resolution, in that instead of an ensemble of "relaxed", fairly smooth condensations one sees a great deal of highly filamentary structure, a strong suggestion of cavities and surrounding regions with enhanced column densities. The large size of the region covered also suggests relationships between the different portions of the Taurus molecular region. The most striking of these points will be addressed briefly later in this paper.

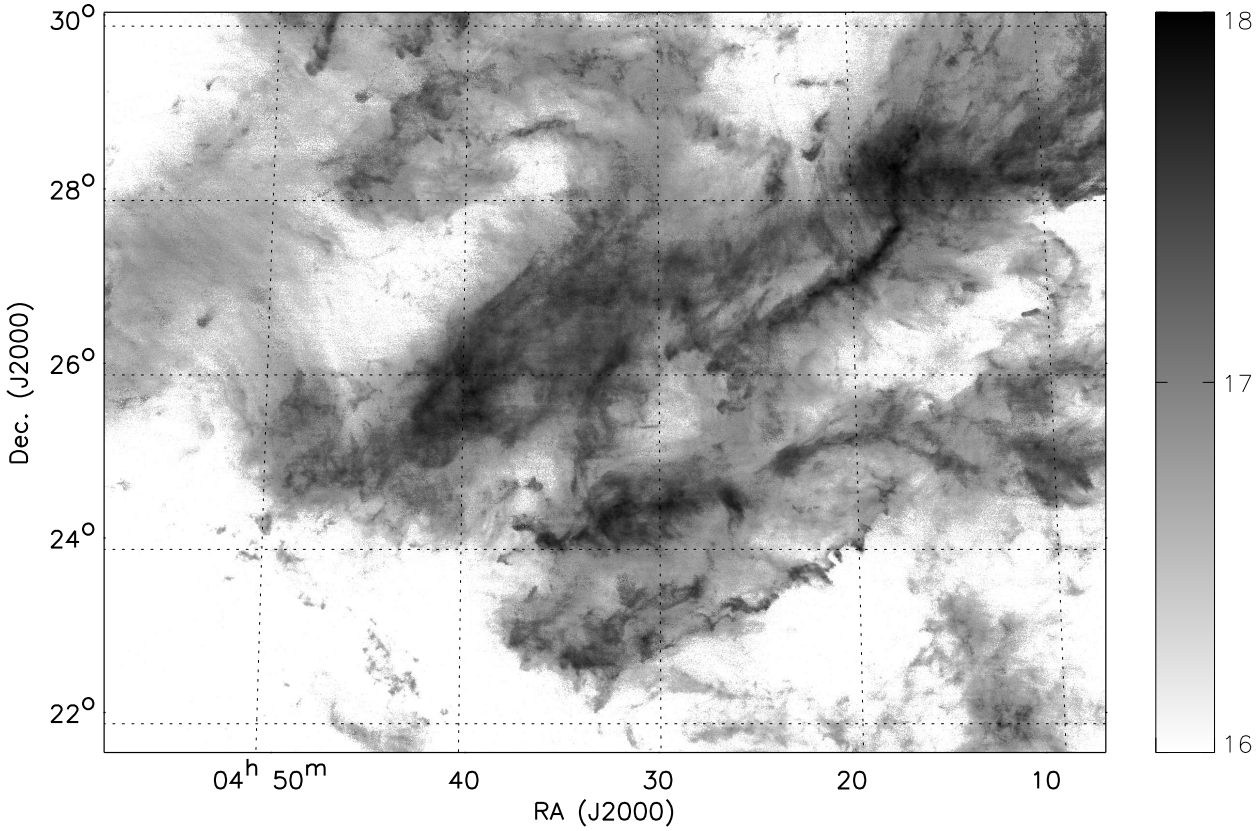

Fig. 7.— Distribution of carbon monoxide in Taurus region expressed as the logarithm of the ^{12}CO column density (cm^{-2}) in mask 1 and mask 2 regions. The scale is indicated by the bar on the right hand side. The ^{12}CO column density in the mask 0 region (indicated by light grey density) is $7.5{\times}10^{15}$ cm^{-2}, as discussed in the text. The maximum ^{12}CO column density is a factor of $\simeq$ 100 larger.

3.2.2. Molecular Hydrogen Column Density and Mass

Most studies of molecular regions using carbon monoxide have emphasized regions in which the column density is sufficiently large that dust shielding plus self–shielding result in an "asymptotic" ^{12}CO abundance between 0.9×10^{-4} and 3.0×10^{-4} relative to H_2 (see e.g. Frerking, Langer, & Wilson 1982; Lacy et al. 1994). In our study of Taurus, only the mask 2 region is plausibly consistent with this assumption. The remainder of the cloud is characterized by lower densities and column densities, and the fractional abundance of carbon monoxide must be regarded as being significantly uncertain and likely to be dependent on the extinction.

There is considerable value in trying to make a self–consistent model for the carbon monoxide as a tracer of total molecular (H_2) column density. To this end, we have used the theoretical modeling by Van Dishoeck & Black (1988). We have utilized the curve for $I_{UV} = 1.0$ (in units of Habings), carbon depletion $\delta_C = 0.1$, and models T1–T6, which correspond to temperature range 40 K to 15 K and $n_H = 500$ cm^{-3} to 1000 cm^{-3} throughout the model slab being considered. We have used a polynomial fit to the data from the appropriate curve in Figure 8 of Van Dishoeck & Black (1988) for the relationship between CO and H_2 column densities. This value of carbon depletion is recommended by Van Dishoeck & Black (1988) as agreeing with the available Taurus data. We also note that the carbon monoxide fractional abundance as given by these models of Van Dishoeck & Black (1988) agrees well at low column densities with the UV measurements of Sonnentrucker et al. (2007) and Burgh et al. (2007).

The lower CO lines in absorption from diffuse clouds lying in front of millimeter continuum sources have been observed by Liszt & Lucas (1998). The clouds, analyzed by Liszt (2007) have a range of H_2 column density (determined by UV absorption; Federman et al. 1994) which extends from 5×10^{20} cm^{-2} to just above 10^{21} cm^{-2}, and thus includes our mask 0 (and very low end of mask 1) results. While there is considerable scatter among various clouds having the same hydrogen column density, the best fit relationship gives $X(^{12}\mathrm{CO}) = 5\times10^{-6}$ for $N(H_2) = 10^{21}$ cm^{-2}. This is quite close to our results and again reinforces the general applicability of a reduced carbon monoxide fractional abundance for low extinction cloud material. The specific parameters we have adopted have been chosen, in addition to being consistent with the measurements of low column density diffuse clouds, to give good agreement at high column densities with the mm emission measurements of Bachiller & Cernicharo (1986), Cernicharo & Guélin (1987), and Alves, Lada, & Lada (1999).

The strong dependence of CO column density on H_2 column density reflects the onset of self–shielding when N(CO) reaches $\simeq10^{15}$ cm^{-2}. This produces a rapidly increasing CO fractional abundance as a function of H_2 column density in the range covered by the mask

0 and mask 1 regions of our study, and a gradual leveling out of N(CO)/N(H_2) in mask 2. The most significant difference is that using this approach we find that the low CO column densities correspond to considerably larger H_2 column densities than would be found if a constant fractional abundance of CO were adopted. We convert our CO distribution to a molecular hydrogen distribution using the nonlinear relationship, and the result is given in histogram form in Figure 8.

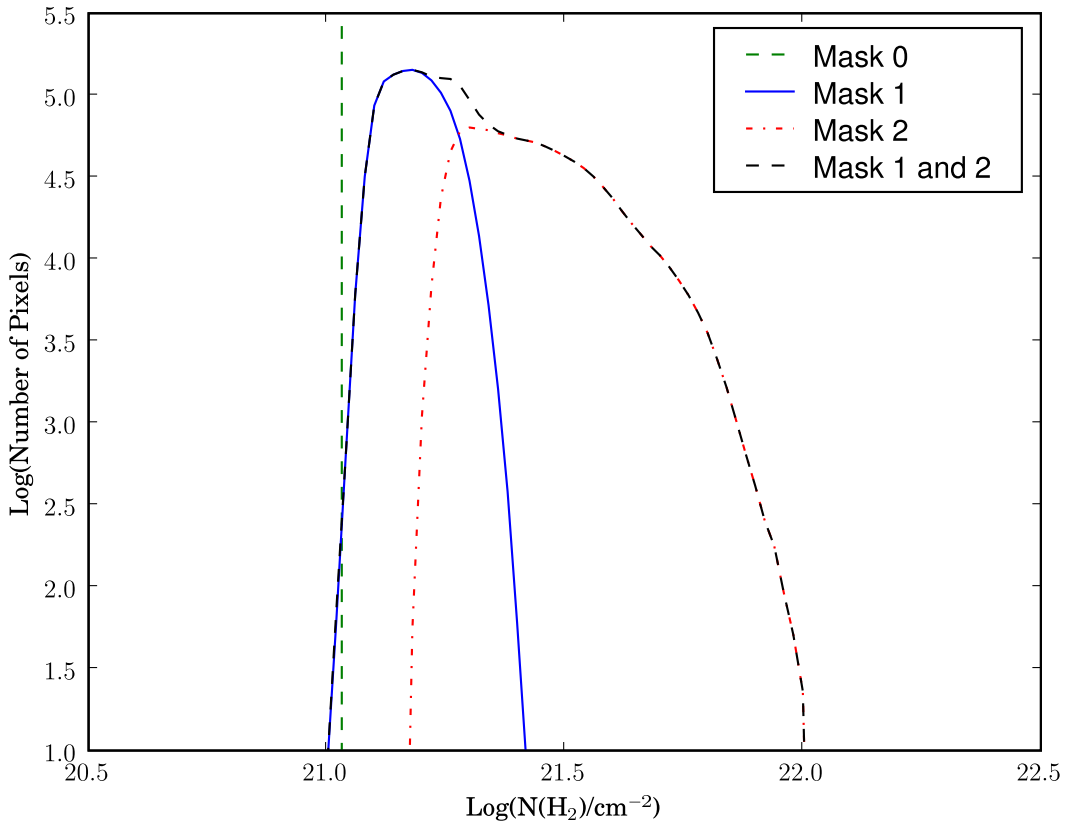

Fig. 8.— Histogram of H_2 column density distribution in Taurus. The distribution of column density in the mask 0 region is given by the vertical (dashed) line, in the mask 1 region by the solid (blue) curve, in the mask 2 region by the dot–dashed (red) curve, and in the combination of the two regions by the long–dashed (black) curve.

When compared to Figure 6, it is evident that the varying fractional abundance has resulted in a significant compression in converting the carbon monoxide to H_2 column densities. The drop in X(CO) in regions of lower extinction and lower density means that the relatively weak emission that we observe there implies a greater H_2 column density than would be derived assuming a constant fractional abundance. Taking mask 0 as an example, the CO

column density of $7.5{\times}10^{15}$ cm^{-2}, with fractional abundance $7.0{\times}10^{-6}$ corresponds to an H_2 column density equal to $1.1{\times}10^{21}$ cm^{-2} using the variable fractional abundance, more than an order of magnitude larger than would be obtained using the canonical high–extinction fractional abundance of 10^{-4}.

This suggests that the majority of the area within the Taurus molecular cloud complex has a visual extinction from molecular hydrogen on the order of 1 magnitude. This is consistent with the hydrogen column density of mask 1 discussed in the previous section, as well as with the "halo" component of the HCL2 region discussed by Cernicharo & Guélin (1987). There is certainly a high column density tail which reaches 10^{22} cm^{-2}, but this includes only a very small fraction of the cloud area and mass. While ^{13}CO is not the ideal tracer of the densest component of the cloud, this study makes it clear that only about 10^{-3} of the pixels with ^{12}CO detectable have $A_v \geq 5$.

Despite the relatively low density in mask 0 and mask 1 regions, the time scale to arrive at the the low fractional abundance of carbon monoxide found there is quite modest. Using the expression from Section 4.1 of Liszt (2007), we find that if we start with $X(e) = 10^{-5}$ and $n(H_2) = 100$ cm^{-3}, the characteristic time to reach $X(CO) = 10^{-5}$ is only $\sim 10^5$ yr. This is consistent with results obtained using explicit time–dependent models with CO formation and destruction by E. Bergin (private communication). Thus, whatever the history of the diffuse surroundings of dense clouds, the low but significant abundance of carbon monoxide found there appears entirely plausible.

We show the spatial distribution of H_2 column density in the Taurus region mapped in Figure 9. The contributions of individual pixels in mask 1 and mask 2 are included. Approximately 50 percent of the total molecular mass of the region is in directions in which ^{13}CO cannot readily be detected in an individual map pixel. From the masses in each mask region, we compute the total mass of the region of Taurus mapped in the present study. The results (including correction for He and heavy elements) are given in Table 3. For mask 0, we have considered the entire area it comprises to be characterized by the single set of conditions derived in the previous subsection, while the contribution of mask 3 has been neglected.

Table 3 shows that assuming the physically plausible variable fractional abundance of carbon monoxide gives a total mass of the region a factor approximately 2.5 times larger than that obtained using a uniform high abundance characteristic of well–shielded regions. We also see that the contributions from the low column density mask 0 and mask 1‘ regions are considerably enhanced and that their contribution to the total mass is no longer negligible as would be the case if a constant fractional abundance obtained.

Table 2. ^{12}CO Excitation Temperature Bins in Mask 1 and Best Estimates of Their Characteristics[1]

T_{ex} K	$^{12}CO/^{13}CO$ Observed	Number of Pixels	$n(H_2)$ cm^{-3}	$N(^{12}CO)/\delta v$ 10^{16} cm^{-2}/kms^{-1}	$^{12}CO/^{13}CO$ Abundance Ratio
4.5	21.7	32321	125	0.7	30
5.5	21.7	113923	200	1.0	35
6.5	19.6	202328	250	1.4	38
7.5	16.7	245949	280	2.0	40
8.5	14.9	211649	325	2.7	42
9.5	13.9	175431	425	3.1	45
10.5	13.4	122423	550	3.6	50
11.5	13.0	65428	850	3.7	55
12.5	12.8	27387	1200	4.3	65

[1]The last three columns are model values.

Table 3. Mass of Region in Taurus Mapped

Mask Region	Mass (10^3 $M_\odot$) a	b
0	0.1	4.1
1	1.7	7.7
2	7.8	11.8
Total	9.6	23.6

[a]Using constant H_2/CO ratio equal to 2×10^4

[b]Using H_2/CO ratio with I(UV) = 1.0 and $\delta_C = 0.1$ from Van Dishoeck & Black (1988)

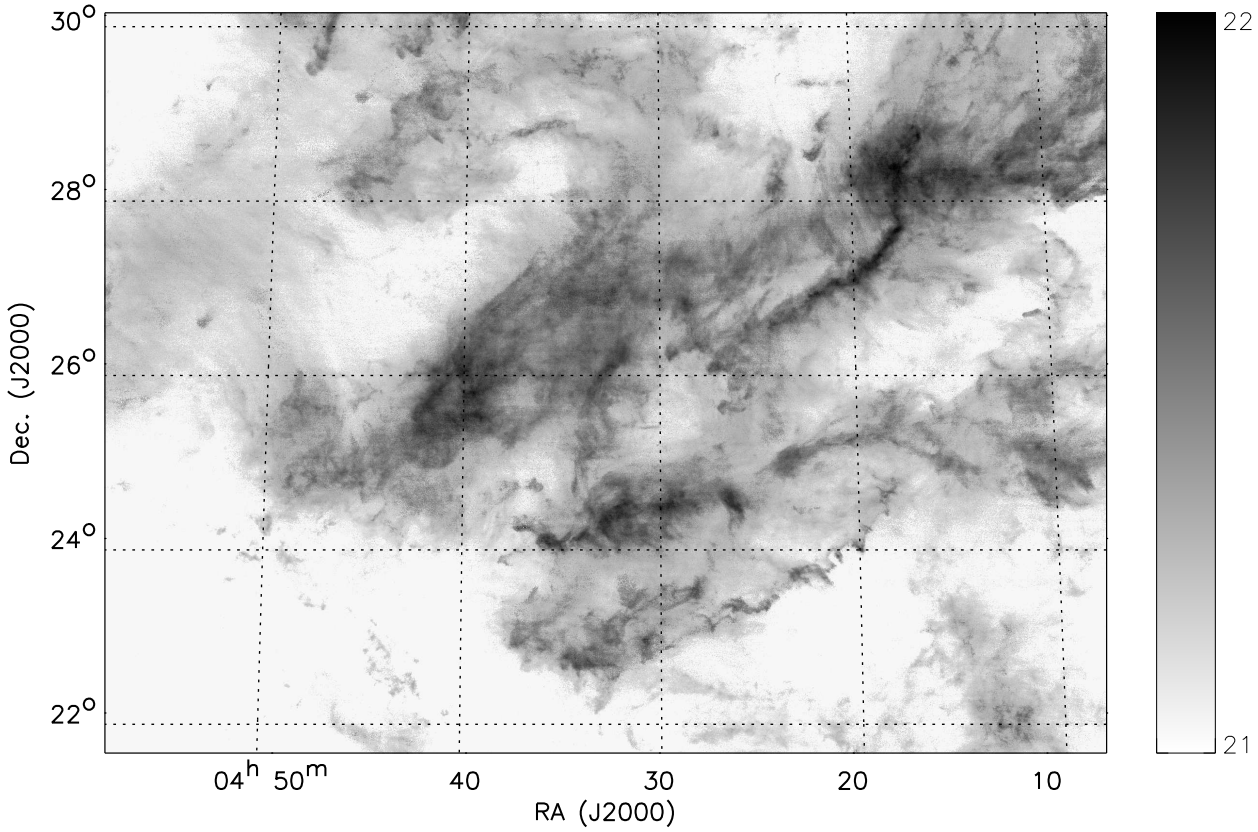

Fig. 9.— Image showing the molecular hydrogen column density distribution derived from mask 0, mask 1, and mask 2 regions in Taurus. The scale is indicated by the bar on the right, expressed as the logarithm of the derived H_2 column density in cm^{-2}.

3.3. Cloud Structure

Valuable insight into the structure of the cloud can be obtained by examining the cumulative distribution of cloud mass and area as a function of column density. This information in shown in Figure 10. Our survey focused on the region of the Taurus molecular cloud known to have most prominent high density regions with exceptional chemical diversity (TMC-1; Pratap et al. 1997) and prominent star formation (e.g. L1495). Nevertheless, we see that half of the cloud's mass is in material with $N(H_2)$ less than 2.1×10^{21} cm^{-2}. Only about 5% of the cloud's mass occurs at H_2 column densities above 5×10^{21} cm^{-2}, or visual extinction greater than 5. The column density we derive may be modestly underestimated due to incomplete correction for saturation in our ^{13}CO observations for large column densities, and as a consequence of molecular depletion at high densities, but even together these effects are unlikely to increase this fraction by a factor of 2 (see e.g. Alves, Lada, & Lada 1999). The fraction of the cloud area with $N(H_2) \geq 5\times10^{21}$ cm^{-2} is only 0.02.

Another view of the mass distribution can be obtained by attempting to dissect the cloud by extracting the well–recognized high column density regions from the remainder of the gas. In Figure 11 we show the division into eight regions, which together include approximately 25% of the area of the map. We have generally followed the region limits and designations given in Fig. 3 of Onishi et al. (1996).

We give the mass of each of these regions in Table 4. The total mass contained in these regions, 9807 $M_\odot$, is 42% of the total mass included in the region we have studied, and their combined area is 21% of that of the region we have mapped. However, since we have made an unbiased map of ^{13}CO rather than a map restricted to regions of strong intensity (as Mizuno et al. 1995, did in their ^{13}CO survey), we include somewhat larger areas. The masses we derive for L1495/B213 and for B18 are approximately a factor of 3 larger than those obtained by Mizuno et al. (1995), and that for HCl2 is a factor of 2 larger. It is evident that a large fraction of the mass even within the boundaries shown in Figure 11 is in relatively low–density gas.

Having a well–sampled ^{12}CO map of a large region and a mass determination allows us to examine the application of a CO luminosity to mass conversion factor (Dickman, Snell, & Schloerb 1986) to Taurus. In Table 5 we show the results for the different mask regions and the total. The entries in the third column are obtained using a conversion factor $M(M_\odot) = 4.1 L_{CO}$(K km s^{-1} pc^2). This value is obtained using the Egret γ–ray data (Strong & Mattox 1996), and a factor 1.36 for the total mass per H_2 molecule (including He and metals) in the gas. For mask 0, the CO luminosity drastically underestimates the mass, due to highly subthermal excitation of the CO and its modest optical depth. For the denser regions, the agreement is much better. The surprisingly close agreement for the complete Taurus region

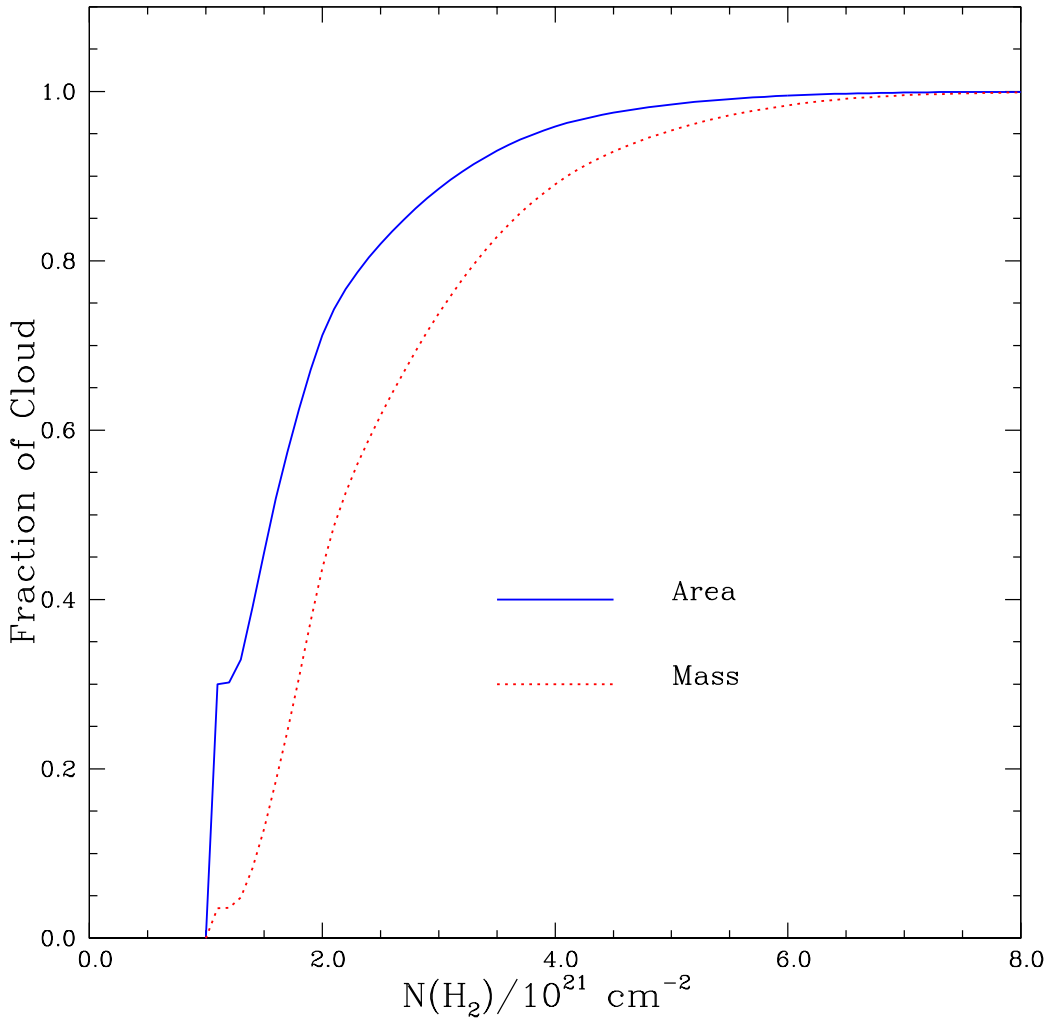

Fig. 10.— Cumulative fraction of Taurus as a function of molecular hydrogen column density. The solid (blue) curve gives the fraction of the area characterized by column density less than specified value, and the dotted (red) curve gives the fraction of the mass similarly characterized. Half the area mapped has column density below 1.6×10^{21} cm^{-2}, and half the mass of the cloud is included in regions having column density below 2.1×10^{21} cm^{-2}.

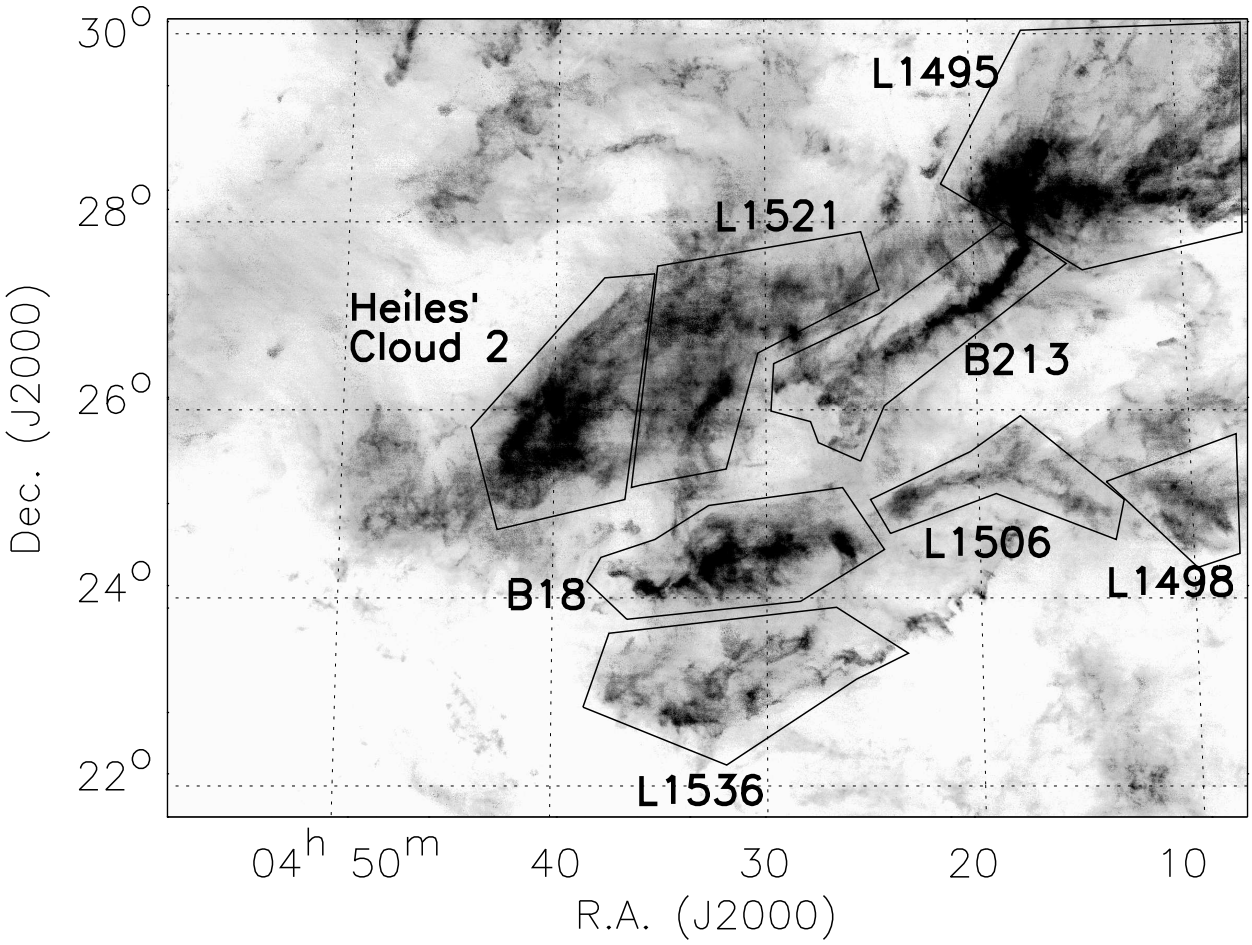

Fig. 11.— Image showing H_2 column density overlaid with the eight well-known regions of high column density as designated by Onishi et al. (1996). These regions define the masses and areas given in Table 4.

Table 4. Mass of High–Density Regions in Taurus[a]

Region	Mass [b] $M_\odot$	Area pc^2
L1495	2616	31.7
B213	1095	13.7
L1521	1584	17.6
HCl2	1513	15.8
L1498	373	5.7
L1506	491	7.7
B18	1157	14.5
L1536	978	16.6
Total	9807	123.3

[a]Regions defined in Figure 11

[b]Includes correction for He

may, to a certain extent, be fortuitous, but it suggests that use of the ^{12}CO luminosity to derive total mass of molecular regions does appear to work reasonably well for regions with only low–mass young stars, as well as for regions with young high–mass stars.

4. LARGE SCALE KINEMATICS OF THE MOLECULAR GAS

Previous studies have revealed a variety of motions on different scales within the Taurus complex. These include velocity gradients along individual filaments possibly indicative of rotation, along with a systematic East–West velocity difference as one moves across the region. In Figure 12 we show a color–coded image of the integrated intensities in three velocity intervals for the two isotopologues. There is a great deal of structure seen even in this relatively crude representation of the velocity field. Certain regions, and particularly the edges of particular regions, show up as having significantly shifted velocities relative to the surrounding gas.

This coarsely divided integrated intensity does not give the full measure of the complexity of the ^{13}CO and ^{12}CO line profiles in Taurus. An indication of this can be seen in Fig. 20 of Narayanan et al. (2007), in which it is evident that in general the regions with multiply–peaked lines exhibit this characteristic in both ^{12}CO and ^{13}CO. Since the visibility of the multiple peaks is approximately equal in the two isotopologues, it is unlikely to be a result of self–absorption, but rather an indication of multiple, kinematically distinct components. These are most prominent in several regions of Taurus, notably the western part of B18, north of L1521, in B213 and west thereof, and in the southern part of Heiles' Cloud 2. This indicates that some regions are characterized by a considerably greater degree of velocity multiplicity along lines of sight. There does not appear to be any correlation of this characteristic with e.g. star formation.

5. MOLECULAR GAS AND THE MAGNETIC FIELD

The Taurus Molecular Cloud has long been a target for investigations of the interstellar magnetic field and its role within the dynamics of the molecular gas component (Moneti et al. 1984; Heyer et al. 1987; Heyer 1988; Goodman et al. 1992; Troland et al. 1996; Crutcher & Troland 2000). Many of these studies have compared the distribution of gas and dust with respect to the magnetic field geometry inferred from optical polarization measurements of background stars. The relationship of the cloud geometry to the magnetic field morphology is an essential aspect of models that have been developed for the formation

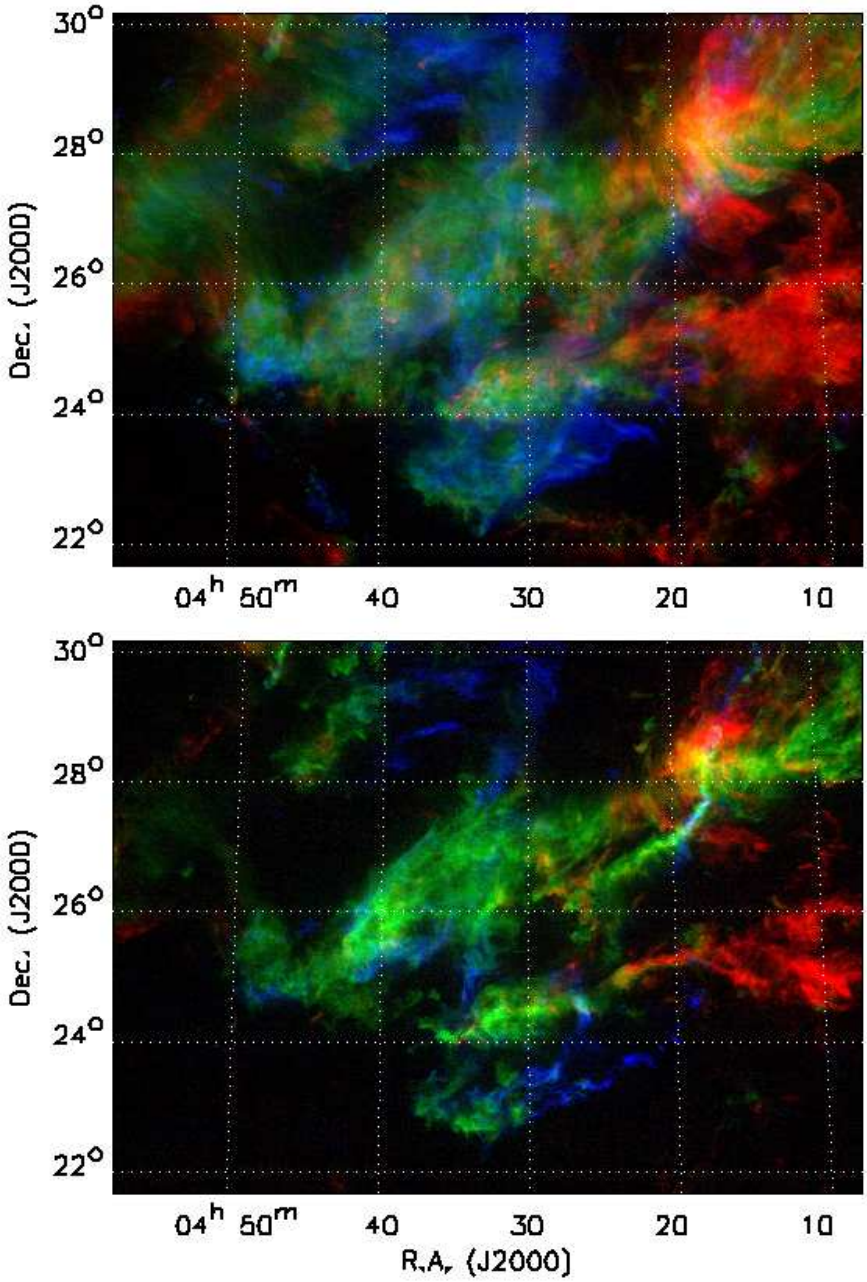

Fig. 12.— Color–coded image of the integrated intensities in three velocity intervals of carbon monoxide in Taurus, with emission at velocities between 3 km s^{-1} and 5 km s^{-1} coded blue, between 5 km s^{-1} and 7 km s^{-1} coded green, and between 7 km s^{-1} and 9 km s^{-1} coded red. Upper panel: ^{12}CO with blue– and red–coded intervals scaled to 7.5 K kms^{-1} and the green–coded interval scaled to 15 K kms^{-1}. Lower panel: ^{13}CO with blue– and red–coded intervals scaled to 5.0 K kms^{-1} and the green–coded interval scaled to 2.5 K kms^{-1}.

of Taurus (Gomez de Castro & Pudritz 1992; Ballesteros-Paredes, Hartmann, & Vázquez–Semadeni 1999). These have hypothesized an initial alignment of a more diffuse cloud with the Galactic magnetic field as part of the initial conditions for formation of the dense cloud, with the gas streaming along magnetic field lines.

Observationally, at intermediate scales ($\sim$1 pc), the situation has become more complex. In particular, toward the western end of the Taurus cloud, the long axis of the L1506 filament is oriented along the field in contrast to alignments of Heiles' Cloud 2 and the B216 and B217 filaments for which the field is essentially perpendicular to the axis of the filaments (Goodman et al. 1992). Note that the latter structure is denoted B213 in Figure 11. From this departure from rigorous alignment, Goodman et al. (1992) conclude that either the magnetic field does not dominate the cloud structure at these scales and densities, or that the optical polarization measurements probe a volume that is spatially distinct from the dense filaments. Goodman et al. (1992) demonstrate that polarization by selective absorption at optical and infrared wavelengths is produced by dust grains within the outer, low column density envelopes of the molecular clouds and provides little or no information on the magnetic field direction within the high density filaments.

The ^{12}CO and ^{13}CO data presented in this study afford an opportunity to extend these comparisons to lower column densities than these previous investigations. We have used the data assembled by Heiles (2000), taken from other sources, and superimposed this on a figure showing the integrated intensities of ^{12}CO and ^{13}CO. Figure 13 shows the results. This figure highlights the relationship between the field direction and the morphology of the dense filaments of gas discussed in the references given above.

We can use the ^{12}CO emission to probe the relationship between the lower column density portions of Taurus and the magnetic field. This comparison is shown in the top half of Figure 13. Within the faint, low surface brightness ^{12}CO emission, we see marked striations, which are discussed in more detail in §7.2.6. Remarkably, these features within the Taurus Cloud follow the local orientation of the magnetic field even as the polarization angles vary from a mean of 53 degrees within the northeast corner of the surveyed area, to 81 degrees within the southwest corner. The alignment of these faint features points toward a strong coupling of the gas with the interstellar magnetic field. Such strong coupling may be expected in these low column density regions that are more exposed to the ambient, UV radiation field, which maintains a higher degree of ionization.

The origin of these threadlike features and the mechanism whereby they are aligned with the magnetic field are not established, but we can speculate on several processes that may be responsible. The channel maps of the molecular line emission identify regions of systematic motions over scales from the resolution limit up to $30'$ to $60'$. If the magnetic

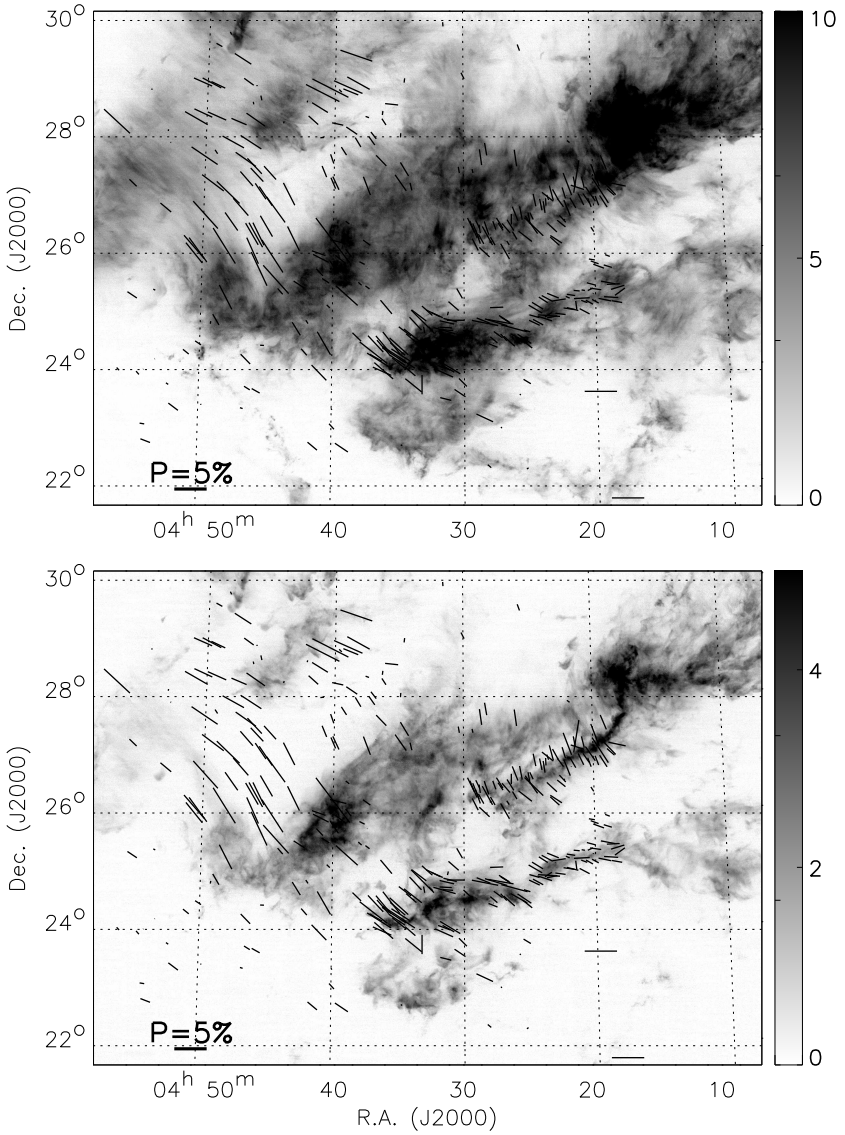

Fig. 13.— Upper panel: magnetic field direction in Taurus superimposed on the ^{12}CO antenna temperature distribution integrated over the 5 km s^{-1} to 8 km s^{-1} velocity range, chosen to emphasize striations and other fine structure. The line segments indicate the direction of the magnetic field derived from observations of absorption by polarized dust grains; their length is proportional to the fractional polarization. The horizontal bar at lower left in each panel indicates 5% fractional polarization. Lower panel: magnetic field direction superimposed on the distribution of ^{13}CO antenna temperature integrated over the same velocity interval. The integrated intensities for each panel in K kms^{-1} are indicated by the bar at the right.

field is well coupled to the neutral gas by frequent ion-neutral collisions but the magnetic energy is small with respect to the kinetic energy of the gas, then the field can be carried by these large scale flows within the cloud. Correspondingly, the field lines would be stretched along the direction of the flow. Alternatively, the narrow emission threads may arise from successive compressions and rarefactions of the gas and magnetic field produced by magnetosonic waves that propagate perpendicular to the field. Within the subthermally excited regime, which likely prevails within these regions of low surface brightness, these column density perturbations would produce corresponding variations in the ^{12}CO intensity.

6. MOLECULAR GAS AND YOUNG STARS IN TAURUS

The distribution of young stellar objects with respect to the molecular gas may offer valuable insights to the formation of stars within a dense interstellar cloud. For comparison with our molecular images, we adopted the set of pre-main sequence stars in the Taurus regions from S. Kenyon (2007 private communication, to be published in 2008). This list is comprised of data from many surveys in optical and infrared wavebands [3]. The pre–main sequence stars are divided into three populations according to their colors. If the R-K magnitude is larger than eight, the star is categorized as likely to be a Class I or younger source. If R-K is smaller than eight, the source is likely to be a T-Tauri star. If the source is not detected in either R or K, it is is likely to be extended/nebulous, in which case it is probably still a protostar, younger than a T-Tauri star. In the region covered by our map, there are a total of 230 stars, 18 of which are Class I or younger, 44 are extended, and 168 are likely to be T-Tauri stars. The stars are shown overlaid on the distribution of the H_2 column density in Figure 14. The distribution of pre–main sequence stars generally follows that of the dense gas, although a many of the stars in the older category are located in regions with only diffuse gas emission. As noted by Hartmann (2002), the young stars are grouped in three nearly parallel bands that are associated with Heiles' Cloud 2/L1521/B213/L1495, B18/L1506 and L1536.

The relationship between H_2 column density and stellar population is examined further in Fig. 15. Roughly equal number of stars can be found in each of the column density bins spanning the range from 0 to 6.5×10^{21} cm^{-2} (upper-left panel). Although the number of stars drops towards higher column density regions, such direct examination of the distribution of stars is somewhat misleading inasmuch as our map includes a substantial area with very

[3]We obtain essentially the same results using the data compiled by F. Palla, which was also provided to us as a private communication.

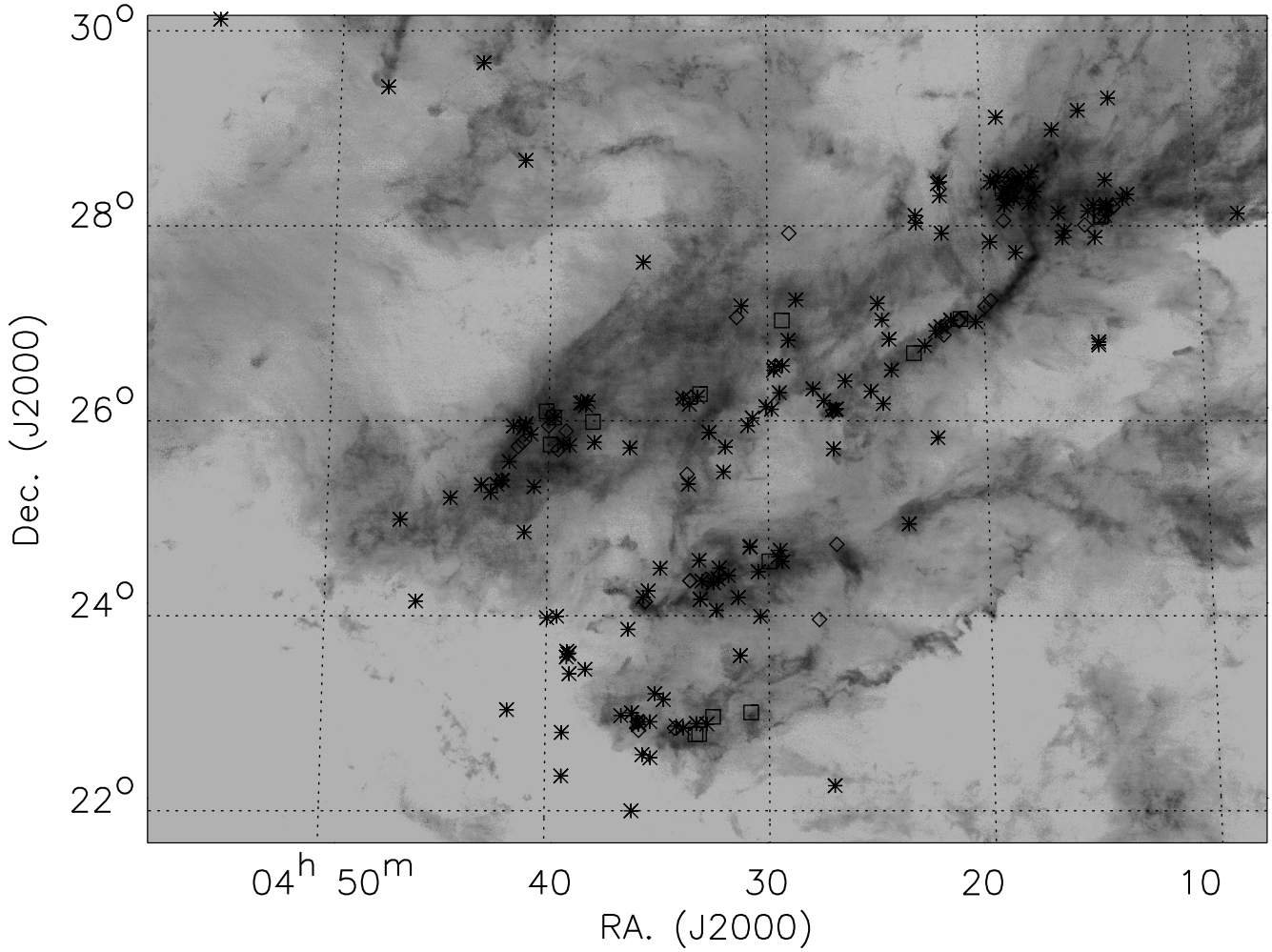

Fig. 14.— Locations of young stars in Taurus superimposed on map of the H_2 column density. The stellar positions are from Kenyon (2007). The diamonds indicate diffuse or extended sources (of which there are 44 in the region mapped), the squares indicate Class I or younger stars (18), and the asterisks indicate T-Tauri stars (168). It is evident that the diffuse and younger sources are almost without exception coincident with regions of relatively large column density, while the older stars show a much larger probability of being found in regions of lower column density.

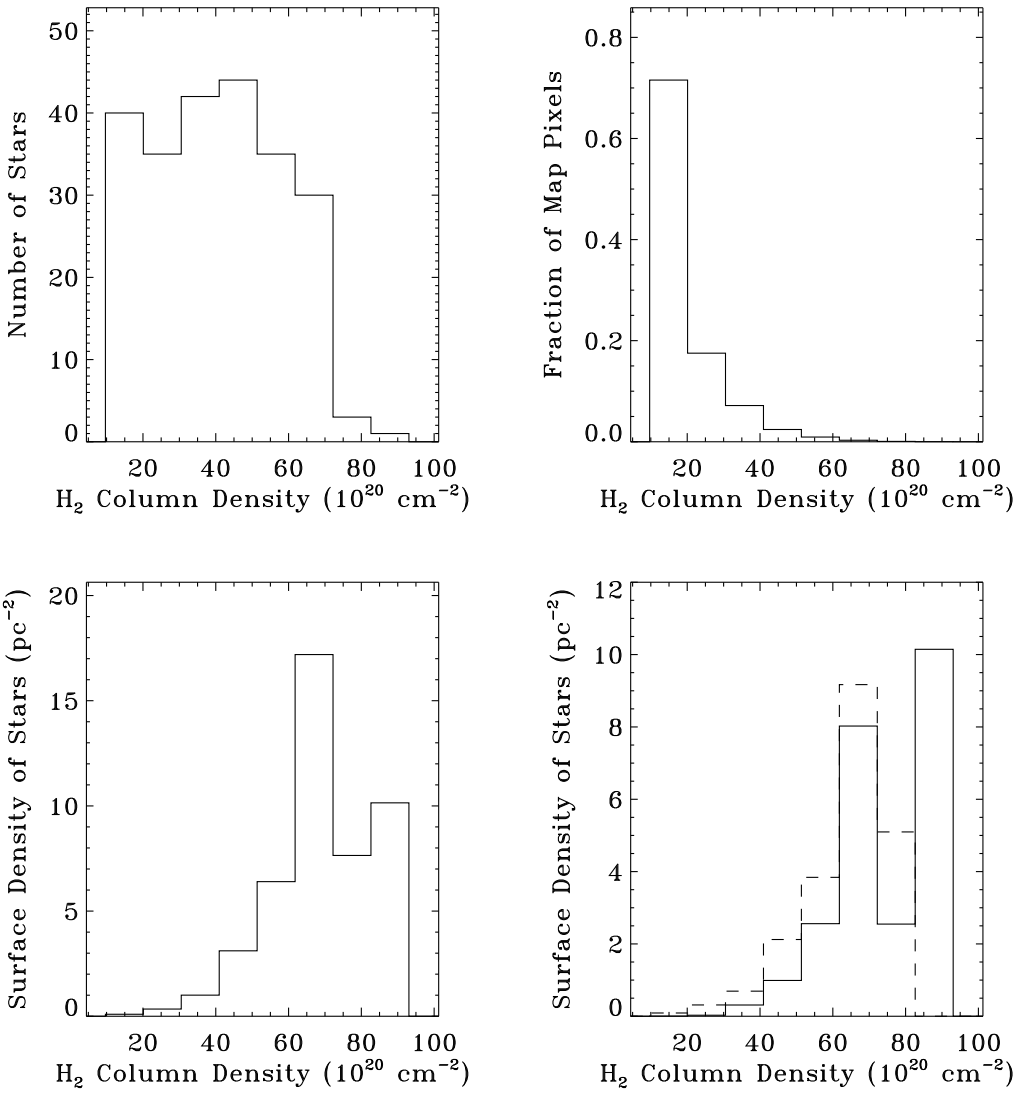

Fig. 15.— Upper left: number of stars as a function of column density. The same bins of column density are used in all panels. Upper right: fraction of pixels in each column density bin. Lower left: surface density of stars obtained by dividing the number of stars in each bin by the area of the map corresponding to each bin. Lower right: surface density of stars in each bin for likely class I and diffuse sources (solid line) and likely T-Tauri stars (dashed line). The division of sources is discussed in the text.

weak or no carbon monoxide emission, as shown in the upper right panel of Figure 15. The surface density of stars versus column density is plotted in the lower left panel. A significant jump in the surface density occurs at around $N(H_2) = 6 \times 10^{21}$ cm^{-2}, or roughly, $A_v = 6$, suggestive of a threshold for star formation. Note that the same trend is visible even in a sample of mostly T-Tauri stars (lower right panel).

In Taurus, neither the dispersion of gas due to star formation nor the dispersion of stars due to stellar motion is likely to have altered the collocation of very dense gas and highly extincted young stars. The threshold in column density for star formation is consistent with the conclusion of Mizuno et al. (1995) with the difference being our finding a higher threshold of 6×10^{21} cm^{-2} instead of 3×10^{21} cm^{-2}. Given the larger number of pre–main sequence stars available for the present work, the significance of the change in the stellar surface density is also higher.

With our rather complete coverage of gas and stars, we can examine the relationship of the stellar mass to the gas mass, which defines the star formation efficiency (or SFE). From a very simplified point of view of the time evolution of the star formation process, we can define the star formation efficiency in three ways. In the first, the SFE is defined as the mass of all known young (pre–main sequence) stars divided by the total gas mass. Assuming an average mass of 0.6 solar mass for each of the stars in our sample (following Palla & Stahler 2000) and the total molecular mass of 2.4×10^4 $M_\odot$ (Table 3), the star formation efficiency thus defined is 0.6 percent.

In the second, we define the SFE more strictly for the current epoch, i.e., counting only the mass of protostars and of dense gas (that in our mask 2 region). The SFE thus defined in this more restricted sense is about 0.3 percent. For the third method, we adopt a less physically motivated but procedurally simple approach of defining the star formation efficiency to be the mass of all pre–main sequence stars divided by the mass of dense gas, we obtain an SFE equal to 1.2 percent. These low values confirm that Taurus is a region of relatively low star formation efficiency.

Since star formation is an ongoing process in Taurus the SFE as defined will evolve with time. A more meaningful quantity is the star formation rate per unit molecular gas mass. The star formation history of Taurus is a topic of some controversy (cf. Palla & Stahler 2000; Hartmann et al. 2001; Palla & Stahler 2002), particularly the issue regarding whether the star formation rate is presently accelerating or has already reached a peak and is declining. Nevertheless, there does seem to be agreement that star formation has been rapid. Star formation in Taurus began over 10 Myr ago, but most of the identified pre-main sequence stars have formed in the past 3 Myr (Palla & Stahler 2002). The average star formation rate over the past 3 Myr within the region of Taurus included in this study has been $\simeq 8 \times 10^{-5}$

stars yr^{-1}.

Assuming as before an average mass of 0.6 solar masses, we derive a star formation rate of 5×10^{-5} $M_\odot$ yr^{-1}. Thus, the star formation rate per unit molecular gas mass is approximately 2×10^{-9} $M_\odot$ per year per solar mass of molecular gas. If this rate were to continue, the gas consumption timescale would be over 400 Myr. However, most of the dense gas is likely to be dispersed by the winds from the newly forming stars long before a significant fraction of the cloud mass is converted into stars. It is intriguing that the star formation rate per unit molecular gas mass in Taurus is very similar to that found globally in the Milky Way (assuming a total molecular mass of 2×10^9 $M_\odot$ and a star formation rate of 3 $M_\odot$ yr^{-1}).

7. MORPHOLOGY OF THE MOLECULAR GAS

7.1. General Structure of the Gas

7.2. Regions of Interest

In this section we discuss several of the regions of particular interest that stand out in the carbon monoxide emission from Taurus. These are to some degree reflections of the complex structure seen on a large scale, but highlight some of the varied structures that can easily be identified. The present discussion is by no means complete but does illustrate the varied and complex structures found in this region in which only low mass star formation is taking place. These are grouped together by location within the cloud so that they can be highlighted by detailed images, but this does not necessarily reflect any physical relationship between different features.

7.2.1. Filamentary Structure Within the Dense Gas

A very striking feature of the molecular gas within the dense portion of Taurus is the fact that the ^{13}CO emission is highly structured even in integrated intensity, as can be seen in Figure 1. An impressive example is shown in Figure 16 which shows a several approximately parallel filaments at $4^h27^m{+}26°45'$, having a southeast to northwest orientation. The filaments are $\simeq$ 20' to 25' (0.8 pc to 1.0 pc) long, with a $\simeq$ 6:1 length to width ratio. These filaments are readily visible in individual velocity images (Narayanan et al. 2007) as well as the ^{13}CO integrated intensity image, but are invisible in the ^{12}CO data. The peak H_2 column density of the filaments is 3×10^{21} cm^{-2}, about a factor of two greater than that of

the region between them.

Another very interesting feature visible in Figure 16 is the almost complete ring–like structure centered at 4^h31^m $+28°01'$. It is fairly circular, having an angular diameter of $18'$, corresponding to 0.73 pc. The molecular hydrogen column density is typically 3×10^{21} cm^{-2} around the periphery of the ring and 1.8×10^{21} cm^{-2} in the center. This ring shows up quite clearly in the ^{12}CO integrated intensity image in which $\int T_A dv$ increases from 7.5 K kms^{-1} in the center to $\simeq$ 11 K kms^{-1} on the periphery. This features is not discernible in the ^{12}CO maximum intensity image, indicating that it is showing increased line width, although distinct kinematic structure is not evident.

7.2.2. Cometary Globules and Ring in Large Cavity

A structure that appears to be a large cavity is visible at the eastern end of B213, just to the north of B18, visible in the ^{12}CO image, but more clearly in the ^{13}CO integrated intensity (Figure 1). An enlarged image is shown in Figure 17. The center of the cavity is approximately $4^h29^m+25°30'$. Although the cavity is still clearly visible, it is considerably smaller, $40'$ (1.6 pc) in ^{12}CO compared to $70'$ (2.9 pc) in ^{13}CO. The minimum H_2 column density of the cavity is 1.4×10^{21} cm^{-3} (it is included in mask 1), but the ^{13}CO is detected when averaged over a reasonable number of pixels.

The boundary of this cavity contains an impressive number of young stars, which in fact nearly completely surround it. To the north, these seem to be distributed around the periphery of the cavity, but at its western edge (the eastern end of B213), there are three prominent condensations, looking remarkably like cometary globules, projecting into the cavity. Some properties of the condensations are shown in Table 6. The globules are undistinguished in terms of maximum ^{12}CO temperature. The maximum column density of each of the globules is close to 4×10^{21} cm^{-2}. We have not been able to identify any source that would be responsible for forming the cavity, but this may be a result of its relatively great age.

As indicated in Table 6 (see also Figure 14), each of the globules contains a T Tauri star, with Globule 2 containing two stars. DF Tau is located slightly inwards (toward the cavity center) relative to Globule 1, while the stars in Globules 2 and 3 are located $3'$ away from the cavity center compared to the tip of the globule. There does not appear to be any readily discernible kinematic signature giving clues to the origin of the globules, or revealing an effect of the star formation. For example, although the star DG Tau B in Globule 2 has an optical jet which is presumed to be driving the observed red–shifted molecular outflow (Mitchell,

Table 5. Comparison of Masses Determined from ^{12}CO and ^{13}CO With Those Derived from CO Luminosity

Region	Mass from ^{12}CO and ^{13}CO ($M_\odot$)	^{12}CO Luminosity (K km s^{-1} pc^2)	Mass from ^{12}CO Luminosity ($M_\odot$)
mask 0	4081	193	791
mask 1	7699	2052	8413
mask 2	11752	3305	13550
Total	23532	5550	22754

Table 6. Properties of Cometary Globules In B213–B18 Cavity

Globule Number	RA(J2000)	Decl(J2000)	Mass $M_\odot$	Embedded Star
1	$4^h26^m49^s.8$	$25°39'06''$	5.9	DF Tau
2	$4^h27^m06^s.3$	$26°06'07''$	8.3	DG Tau
				FV Tau
3	$4^h29^m25^s.5$	$26°14'42''$	4.1	FW Tau

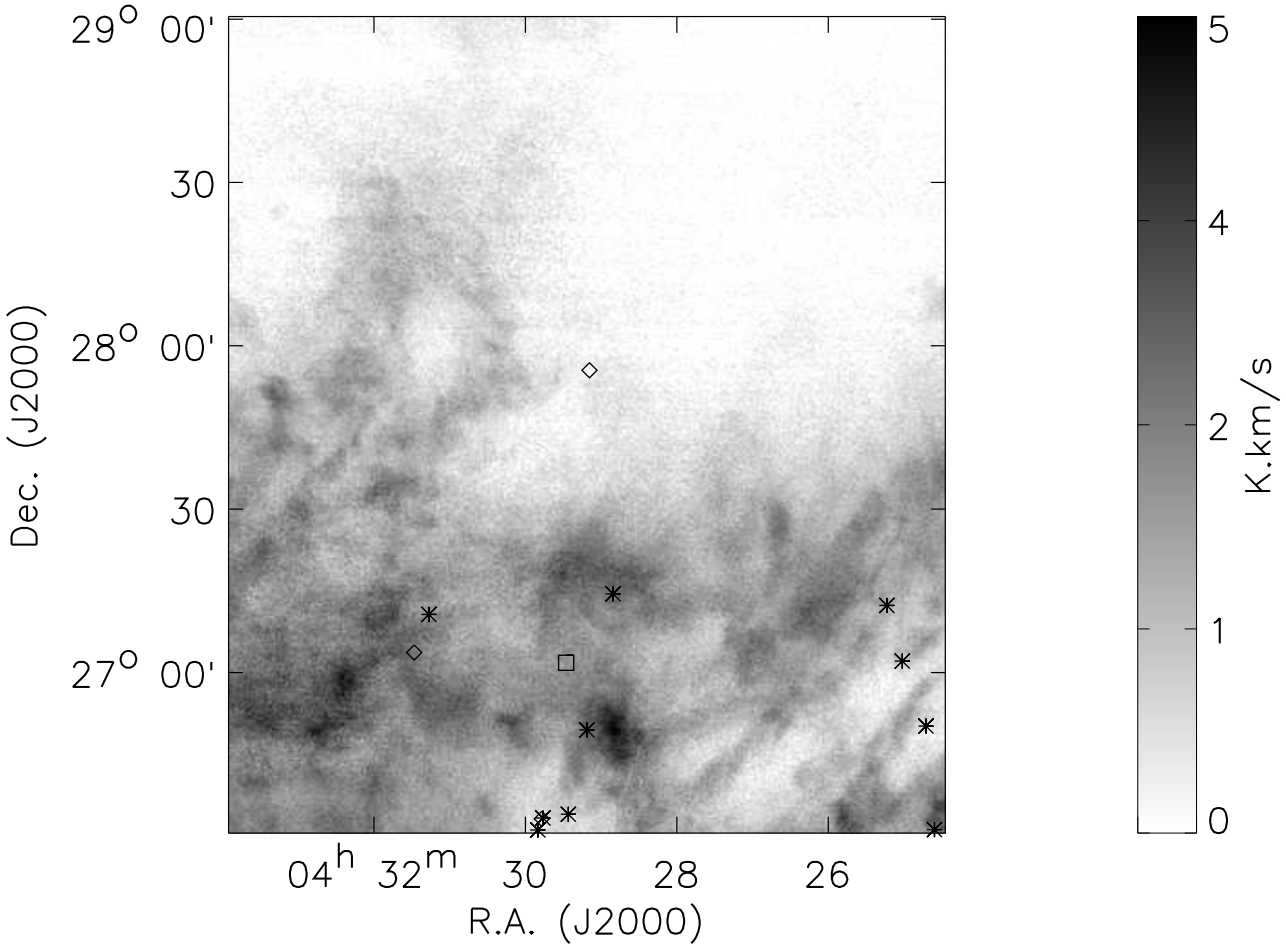

Fig. 16.— Enlarged image of ^{13}CO integrated intensity showing filamentary structures located near $4^h27^m{+}26°45'$. A nearly circular ring–like structure centered at $4^h31^m{+}28°$ is also visible. The young stars in this region are indicated by the symbols defined in Fig. 14. The diamonds indicate diffuse or extended young stellar sources, the square indicates a Class I or diffuse source, and the asterisks indicate T-Tauri stars.

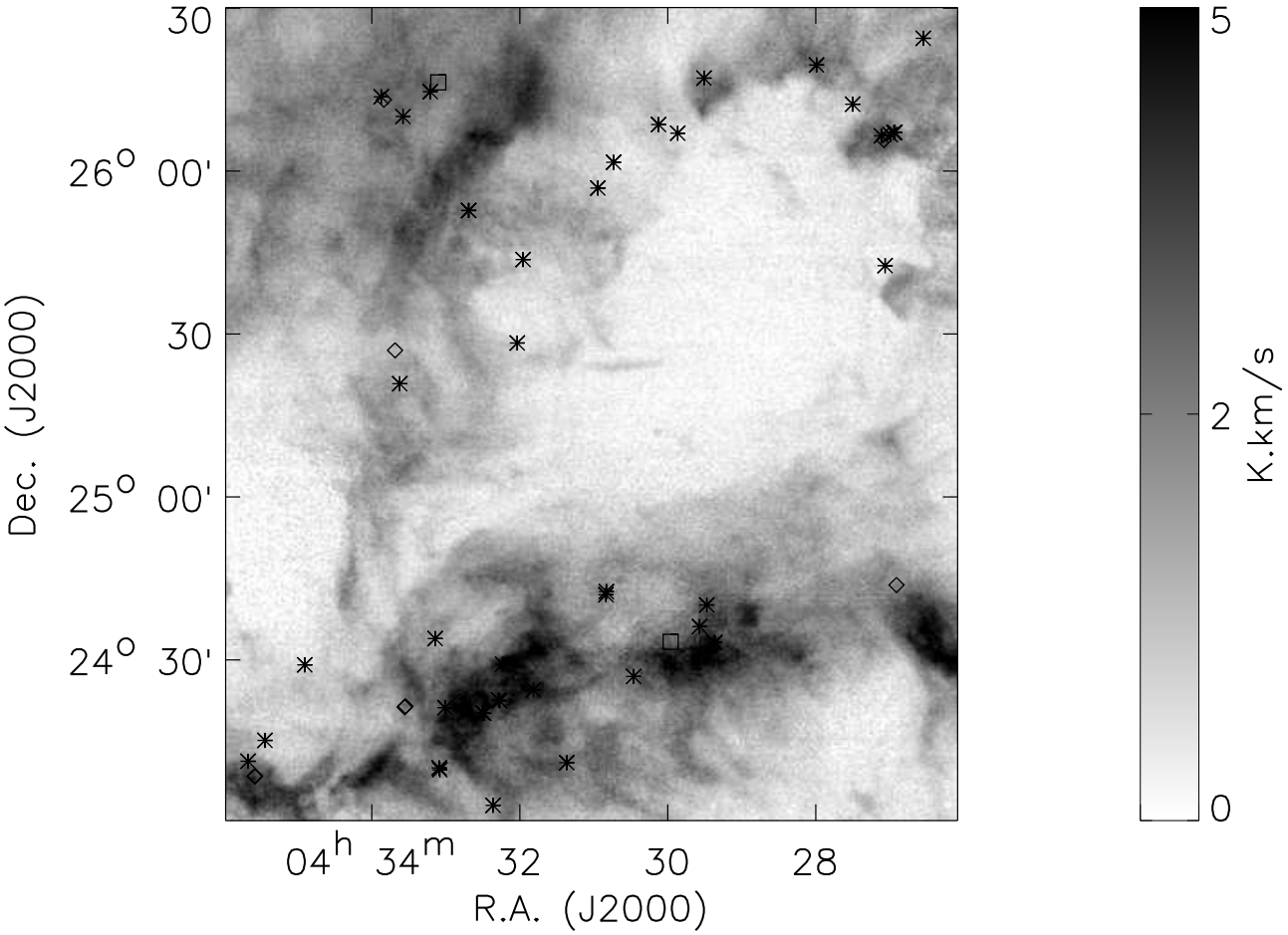

Fig. 17.— This enlarged ^{13}CO integrated intensity image shows the cavity between B213 and B18. At the northwest, three cometary globules are evident, having properties presented in Table 6 and discussed in the text. A nearly complete ring is also seen at the eastern edge of the cavity. The diamonds indicate diffuse or extended young stellar sources, the squares indicate Class I or younger stars, and the asterisks indicate T-Tauri stars.

Sargent, & Mannings 1997), we do not see an effect on the quiescent gas distribution.

The stars in question range from 0.2 $L_\odot$ to 2.2 $L_\odot$, and have ages between 0.6 Myr (DG Tau) to 1.2 Myr (FW Tau). Stars of this age may well have moved a significant distance since their formation, so that it is not surprising that if they were formed in these globules by e.g. radiative implosion (Bertoldi & McKee 1990), they may now appear displaced from their formation sites.

7.2.3. Irregular Filament or Boundary in L1536

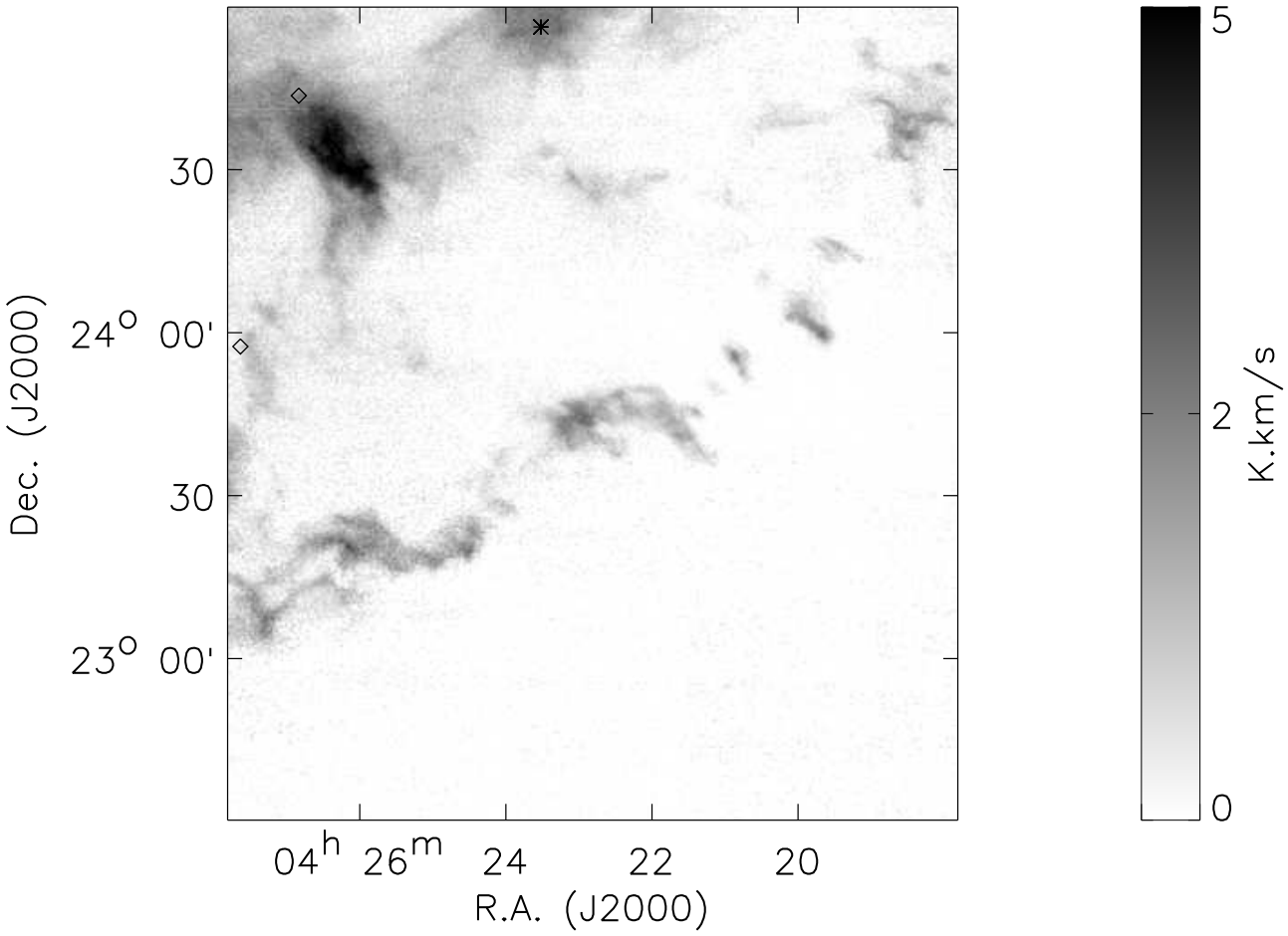

Fig. 18.— Filament running to northwest from L1536 seen in ^{13}CO integrated emission. The condensations have a maximum H_2 column density of 5×10^{21} cm^{-2}. The diamonds indicate diffuse or extended young stellar sources and the asterisk indicates a T-Tauri star.

A very long filament having one end in the south–central portion of L1536 and extending to the northwest is visible in the ^{13}CO emission, shown in an enlarged view in Figure 18. The filament center is at 4^h23^m $+23°45'$, and its length is 2°, corresponding to 4.9 pc. The morphology of the filament is suggestive of its being a boundary between regions of lower (to the south) and higher (to the north) column density. The form of the filament is somewhat suggestive of a helix, but it could simply have an irregular shape. The H_2 column density along the filament is typically 3×10^{21} cm^{-2}, but reaches 5×10^{21} cm^{-2} in the regions of strongest emission. The region surrounding the filament has a H_2 column density of 1.3 to 1.5 $\times10^{21}$ cm^{-2}, only slightly greater than our minimum value defined by mask 0 of 1.1×10^{21} cm^{-2}. This filament, is roughly parallel to the structure formed by B18 and L1506, to the filamentary part of B213, and also to the less well–defined but still quite flattened structure formed by Heiles' Cloud 2 and L1521. This thin filament is the most southerly and furthest from the Galactic plane of all of these structures. The position angle of all four of these filamentary/elongated clouds is approximately 45° relative to the plane of the Milky Way.

7.2.4. Molecular Ring and Planar Boundary

Figure 19 includes several different structures. The first is the "molecular ring", studied in detail by Schloerb & Snell (1984). This ring, 30′ (1.2 pc) in diameter, centered at $4^h40^m30^s$ $+25°45'$, contains at least 6 dense condensations visible in the ^{13}CO integrated intensity image. The best–studied of these is the chemically very interesting TMC-1 ridge, observed in detail by Pratap et al. (1997) and many others. The ridge (the NH_3 peak is at $4^h41^m21^s$+25°48′) is not very prominent in the ^{13}CO integrated intensity image, which is presumably a result of the significant optical depth in the ring material, which may not be corrected for entirely by the simple process (described in §3.2.1) employed here. The peak H_2 column density we derive is 7×10^{21} cm^{-2} which is somewhat less than half of that which would be derived from the C^{18}O observations of Pratap et al. (1997). Given the difficulties expected in deriving the column density in regions of optically thick emission in which significant temperature gradients may be present, this difference is not unreasonable. The ridge is more visible in our ^{12}CO map than in that of Schloerb & Snell (1984) due to the better sampling in the present work.

The second noticeable feature in Figure 19 is the very straight boundary of the molecular emission seen in ^{13}CO centered at $4^h38^m30^s$ $+26°50'$ and extending for over 1 degree (2.4 pc). The questions of the formation of this interface and how it is maintained are intriguing. In this region, the ^{12}CO emission extends significantly beyond that of the ^{13}CO away from the high column density portion of the cloud, typically by 0.5 pc. As can be seen in Figures

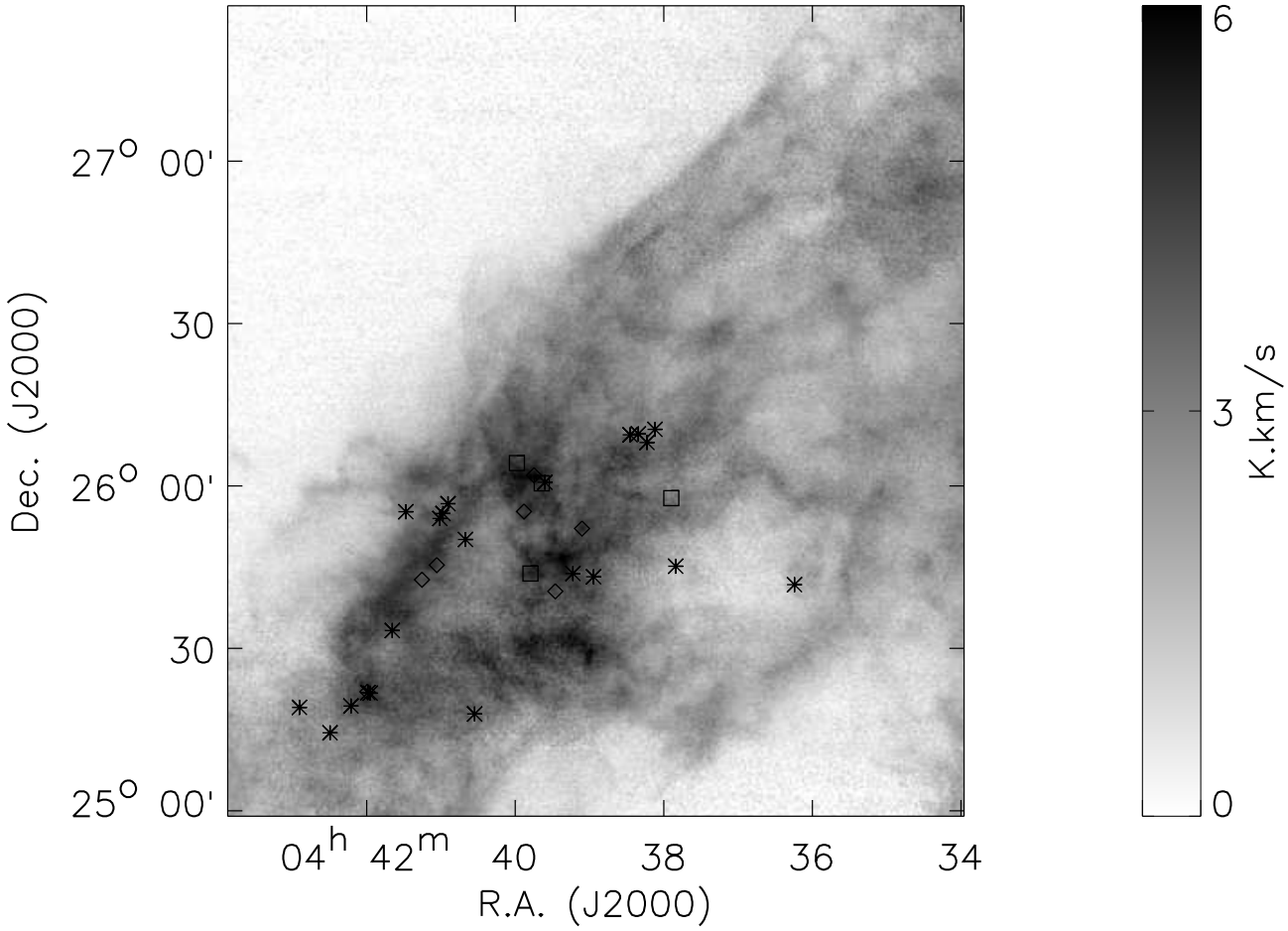

Fig. 19.— ^{13}CO integrated intensity image showing the molecular ring in Heiles' Cloud 2 centered at $4^h40^m30^s$ $+25°45'$. We also see the very well–defined planar boundary centered at $4^h38^m30^s$ $+26°50'$. The ^{12}CO boundary in this region is not at all sharp, having a hair-like appearance as seen most clearly in Figure 13. The diamonds indicate diffuse or extended young stellar sources, the squares indicate Class I or younger stars, and the asterisks indicate T-Tauri stars.

2 and 13, the ^{12}CO emission is highly structured, particularly perpendicular to the interface direction. This behavior is not restricted to this portion of the cloud boundary, but in fact is a general characteristic of the ^{12}CO emission in the mask 1 region surrounding the high column density portion of the cloud (mask 2) where ^{13}CO is detected in individual spectra.

Finally, we note the intriguing feature to the west of the better–known ring discussed above. With a center at 4^h37^m+26°45′, this is again a slightly non circular ring having a diameter of 30′ (1.2 pc). Given the complexity of the structure observed in our study of the molecular gas in Taurus, this could certainly be a superposition of filaments rather than a ring.

7.2.5. L1495 and B213

The L1495 region contains the greatest concentration of young stars within the region of the Taurus molecular cloud that we have mapped. Figure 20 shows the eastern part of L1495; the western part (seen in Figure 1) is more diffuse. The enlarged image also shows the very narrow B213 filament which extends to the southeast from L1495. The ^{13}CO emission and the H_2 column density we derive from it, are relatively continuous over the high column density portion of L1495 and the B213 filament. In C^{18}O (Onishi et al. 1996) individual dense cores are better resolved, and in HCO^+ (Onishi et al. 2002) they stand out yet more clearly.

The central part of of L1495 contains over 20 young stars in Palla's compilation (Palla 2008), and has a maximum H_2 column density of 10^{22} cm^{-2}, which is the highest we see in our map. The mass of the L1495 region is (Table 4) 2.6×10^3 $M_\odot$, but a significant fraction of this is in the spatially extended, lower density material.

The B213 filament is approximately 75′ or 3 pc in length, and only 4.5′ or 0.2 pc thick. One of the curious features about this structure is that while there are dense cores seen along its entire length (Onishi et al. 1996, 2002), young stars have apparently not yet formed in the northwestern 30′ (1.2 pc) long portion closest to L1495. The magnetic field orientation at the boundaries of this filament is strikingly oriented perpendicular to its long axis, as seen dramatically in Figure 13, and discussed in §5.

7.2.6. Striations in ^{12}CO Emission

One of the surprising features in the map of ^{12}CO is the prominent striations (or threads, or strands) seen in the lower level emission seen away from the main molecular condensations.

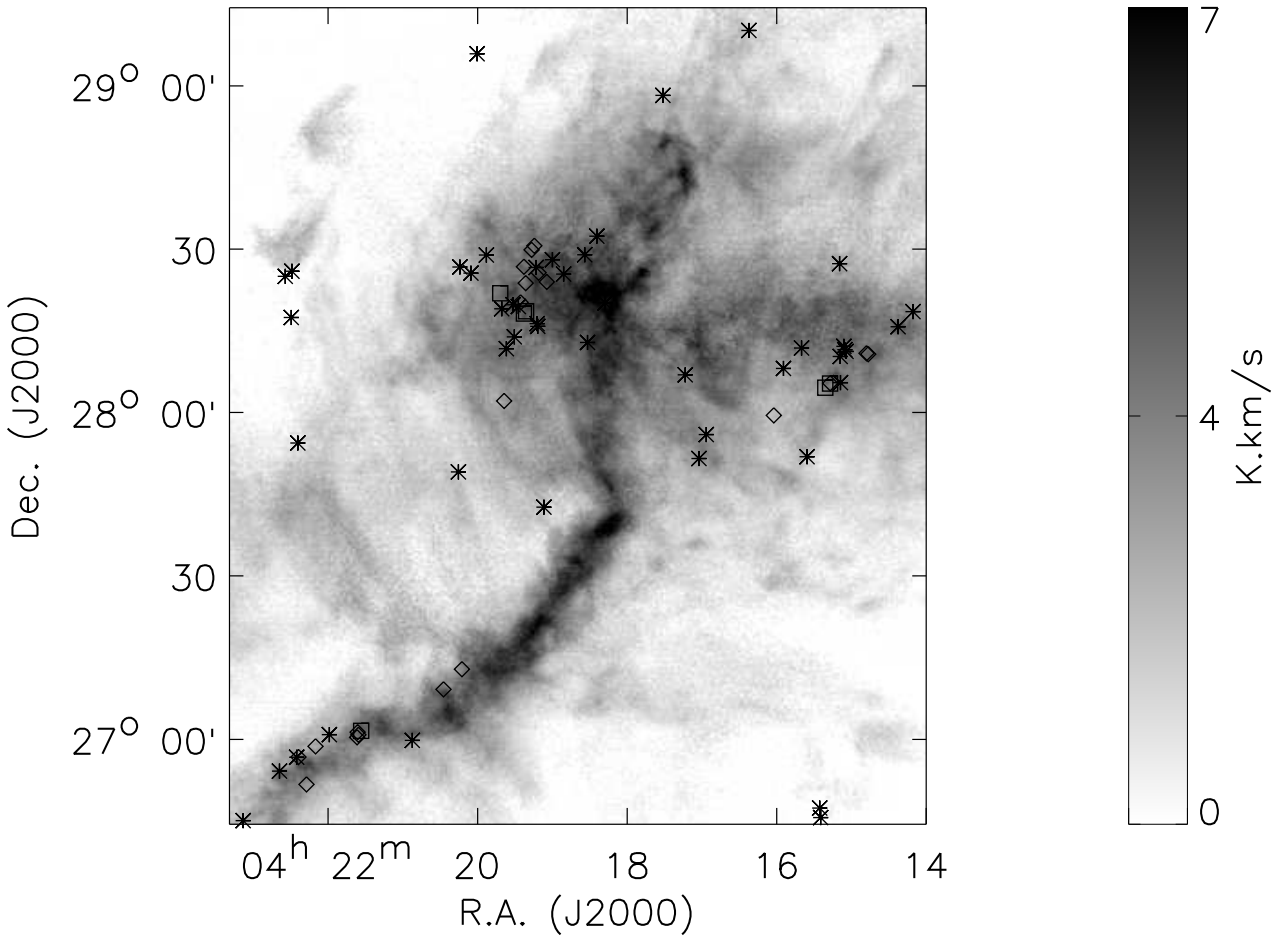

Fig. 20.— Enlarged ^{13}CO integrated intensity image of the western portion of L1495 ($4^h17^m30^s$ $+28°20'$) and the filamentary region B213 (running to the southeast from $4^h17^m30^s$ $+27°40'$. The diamonds indicate diffuse or extended young stellar sources, the squares indicate Class I or younger stars, and the asterisks indicate T-Tauri stars.

These can be recognized in Figure 2, but this effect is more visible in the enlarged image shown in Figure 21. Another region in which this is very prominent is located at 4^h15^m $+24°30'$. These are similar to structures seen within some infrared cirrus clouds. The striations are visible in images of maximum antenna temperature and also integrated antenna temperature. The characteristic values are $T_A = 3$ K on the striations and 2 K between them, while $\int T_A dv$ drops from $\simeq 2.8$ K kms^{-1} on the striations to between 1 and 1.5 K kms^{-1} between them. Given that the density in these regions is low, the ^{12}CO emission is almost certainly subthermally excited so that it is difficult to determine the kinetic temperature. Based on the procedure described in §3.2.1, which assumes T_{kin} equal to 15 K, the H_2 column density of the striated features is 2×10^{21} cm^{-2}, approximately double that of the background emission. A striking feature of the striations is their alignment parallel to the direction of the magnetic field measured by optical starlight polarization, as shown in Figure 13 and discussed in §5.

8. SUMMARY AND CONCLUSIONS

We have carried out a large–scale survey of the molecular gas in Taurus by mapping a 100 square degree region with the 13.7 m Five College Radio Astronomy Observatory millimeter telescope. The J = 1 → 0 transition of ^{12}CO and of ^{13}CO were observed simultaneously using the 32 pixel Sequoia focal plane array receiver. The observing and data reduction techniques are discussed by Narayanan et al. (2007). In this overview, we have discussed some of the highlights of the data that we have obtained, deferring detailed analyses to future papers.

The combination of an unbiased, high sensitivity survey with coverage of a relatively large area allows us to study the structure and properties of the molecular gas in new ways. With approximately 3 million independent spatial pixels, we have a linear dynamic range which is unequaled in previous studies of the Taurus region. While our angular resolution is inferior to that obtained with larger/higher frequency telescopes or interferometers, the strength of the present work is to show the relationship between structures on scales ranging from $\simeq 1'$ or 0.04 pc to 10 degrees (approximately 25 pc). Our observations are sensitive to a range of column densities equivalent to a range in visual extinction between 1 and 10 magnitudes.

Cloud Morphology One of our key conclusions is that the morphology of this region is very complex. In contrast to earlier large–scale surveys carried out with low angular resolution in which clouds appeared largely smooth–edged and having little structure, we find an astoundingly rich range of structures including filaments, ridges, blobs, and holes. The internal structure is more striking in ^{13}CO than in ^{12}CO which is not surprising given

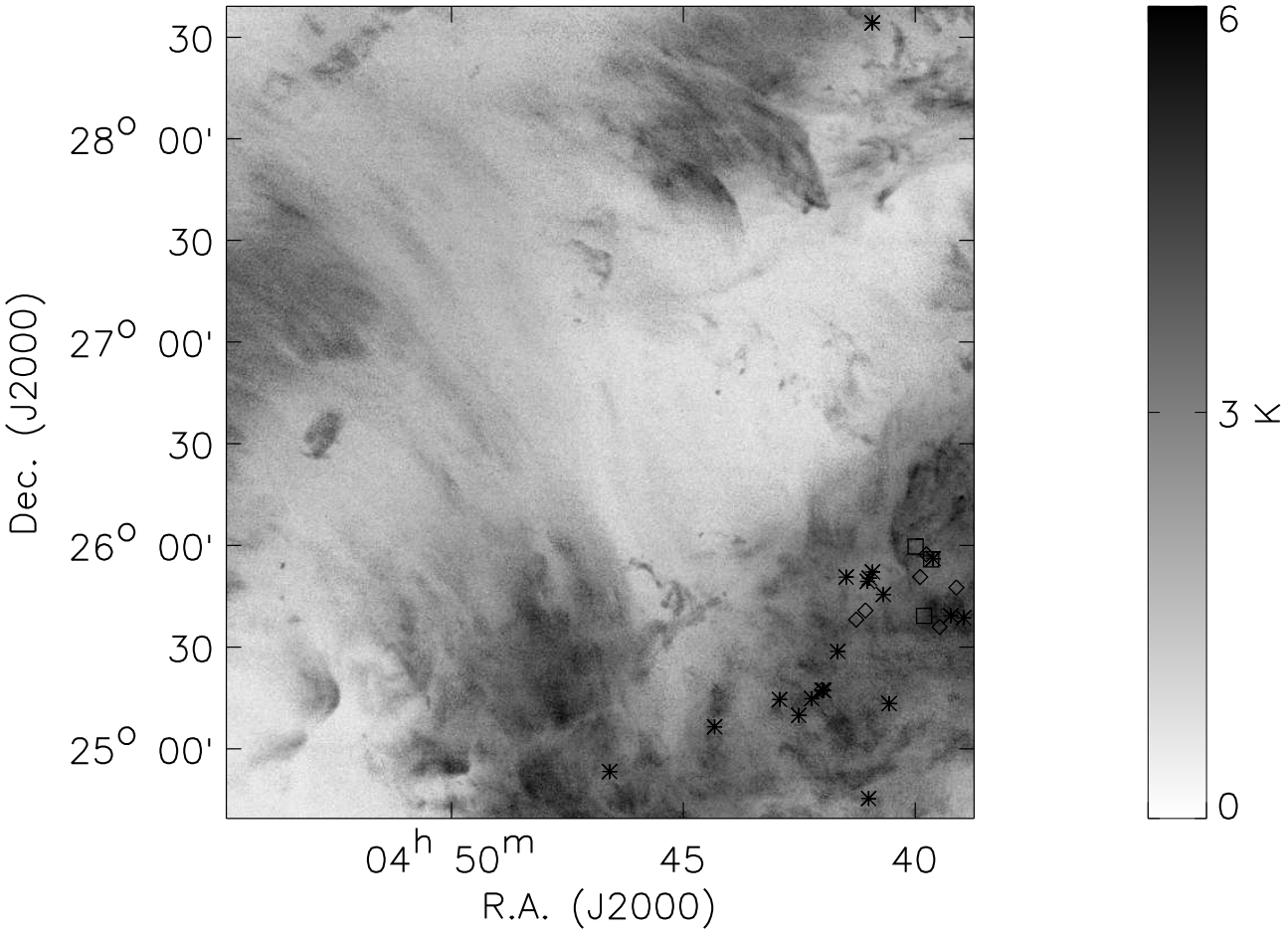

Fig. 21.— One of the regions showing prominent striations in the ^{12}CO emission, displayed here in an image of the maximum ^{12}CO antenna temperature. The diamonds indicate diffuse or extended young stellar sources, the squares indicate Class I or younger stars, and the asterisks indicate T-Tauri stars.

the large optical depth of the former isotopologue. The filaments have lengths up to 3 pc, and axial to transverse dimension ratios as large as 15:1. Holes in the molecular emission appear on a large range of scales extending from 0.1 pc to 3 pc.

The edges of the dense molecular regions are generally very irregular, with structures on the order of 0.1 pc in size visible especially in ^{12}CO which traces cloud boundaries which are more extended than seen in the ^{13}CO. This "hair–like" edge structure is found to be common in ^{12}CO while the ^{13}CO cloud boundaries are relatively sharper but still quite irregular. There is one notable exception in which we find a sharp, straight boundary in ^{13}CO almost 2.5 pc in length.

Cloud Mass and Mass Distribution Having both the ^{12}CO and ^{13}CO detected in regions of relatively large column density (mask 2, comprising about 1/3 of the map pixels), we have used the standard method to derive the kinetic temperature and molecular column density, including a correction for saturation of the ^{13}CO which becomes significant for the regions of greatest column density. To analyze portions of the image (mask 1 comprising about 1/3 of total area of the cloud mapped) in which we detect ^{12}CO but not ^{13}CO in individual pixels we use a different approach. With $\simeq$ 1 million such pixels available, we have binned them by ^{12}CO excitation temperature T_{ex}. When spectra within a bin are averaged, the ^{13}CO as well as the ^{12}CO is readily detectable, and we obtain the H_2 density and the CO column density. We thus have a relationship which gives us n(H_2) and N(CO) as a function of $T_{ex}(^{12}CO)$. Since the excitation temperature is available for each pixel, we can derive the CO column density for each line of sight. Averaging together all the pixels in mask 0 (in any one of which neither ^{12}CO nor ^{13}CO was detectable), we detect both isotopologues, and use the two spectra to derive the average density and column density for mask 0, the final third of the map. This procedure allows us to determine the CO column density throughout the region mapped, including even regions of relatively low column density.

To convert $N(CO)$ to total column density, we have used the results of Van Dishoeck & Black (1988) which are appropriate for Taurus. The essential point is that the fractional abundance of carbon monoxide drops as the total H_2 column density is reduced, as a result of reduced dust shielding and self–shielding. Inverting this argument, the column density of H_2 corresponding to a low column density of carbon monoxide is larger than would be obtained assuming a constant fractional abundance for CO. The result is that the total mass for the region of Taurus mapped is close to 2.4×10^4 $M_\odot$, compared to less than 1×10^4 $M_\odot$ that would be found using a standard, uniform fractional abundance. We find that half the mass of the cloud is contained in regions having column density below 2.1×10^{21} cm^{-2}. This result reduces the fraction of mass found in dense cores by a factor greater than 2, and also confirms the presence of significant external pressure in the regions external to the dense regions. The

total mass for the region we have mapped thus obtained agrees well with that predicted from the CO luminosity, 5.55×10^3 K km s^{-1} pc^2, and a standard conversion M($M_\odot$) = 4.1 L_{CO} (K km s^{-1} pc^2). It seems likely that our conclusion that a significant component of diffuse molecular gas accompanies the more widely studied high density regions is not restricted to Taurus. It reinforces the importance of observations which can study this diffuse molecular material, which is not readily detected in individual spectra with the sensitivity typically available in large–scale molecular cloud surveys.

Cloud Structure and Star Formation The structural complexity over a wide range of scale sizes hints at the richness of the physical processes which underly the formation and evolution of molecular cloud complexes such as Taurus. The present data set, both in terms of morphology and mass distribution, constitutes a potentially valuable resource for comparison with outputs from simulations of cloud formation. The large scale kinematic structure that we see confirms that identified in earlier studies. Along with the complexity of the line profiles observed along many lines of sight, this poses a real challenge for any detailed theoretical model of this region.

We see a varied relationship between the magnetic field as measured by polarization of background stars, and the distribution of the gas. In the more diffuse regions traced by ^{12}CO we see large–scale alignment between the field direction and striated structure in the gas. Although we have not been able to measure any kinematic signature, the appearance is strongly suggestive of flows along the field lines. In several of the very elongated filaments seen in the denser gas traced by ^{13}CO, the magnetic field is oriented perpendicular, or nearly perpendicular, to the major axes of the filaments. Combined with the hair–like appearance of the boundaries of these filaments seen in ^{13}CO but more prominent in ^{12}CO, this again suggests that motions of material along the field lines have been responsible for building up the regions of higher density within the overall molecular cloud.

The surface density of very young and moderately young stars shows a rapid increase at a H_2 column density of 6×10^{21} cm^{-2}, confirming the existence of a threshold for star formation. We have used new compilations of young stars in the Taurus region to calculate the star formation efficiency (SFE). Our large value for the gas mass, especially in regions of lower column density, results in the SFE, taken to be the mass of all young stars in the region divided by the total molecular mass, to be 0.6 percent. Taking the SFE for most recent star formation by comparing the mass of only the embedded protostars with that of the dense gas, gives an SFE equal to 0.3 percent. If we consider all of the young stars (whether embedded protostars or T-Tauri stars) in the region of high column density, we obtain a SFE equal to 1.2 percent. The average star formation rate over the past 3 Myr within the region of Taurus included in this study has been $\simeq 8\times10^{-5}$ stars yr^{-1}, corresponding to a mass going

into new stars of 5×10^{-5} $M_\odot$ yr^{-1}.

This work was supported in part by the National Science Foundation through grant AST-0407019 to Cornell University, and by the Jet Propulsion Laboratory, California Institute of Technology. The Five College Radio Astronomy Observatory is operated with support from the National Science Foundation through NSF grant AST 05 40852 and with permission of the Metropolitan District Commission. We thank Yvonne Tang for contributions to data taking and analysis of dense condensations in Taurus, and Marko Krco for assistance with observations. We thank Pierre Hily–Blant for the suggestion to compare the magnetic field and integrated intensity maps in Taurus, and for many useful conversations about this and other topics. We are indebted to Francesco Palla and Scott Kenyon for providing compilations of young stars in the Taurus region and their properties. We thank Ted Bergin for carrying out time–dependent calculations of the CO abundance in diffuse regions. We thank the anonymous reviewer for very carefully reading the lengthy manuscript, noting some problems, and making some suggestions for further work which has improved this study. This research has made use of NASA's Astrophysics Data System.

REFERENCES

Abergel, A., Boulanger, F., Fukui, Y., & Mizuno, A. 1995, A&A, 111, 483

Alves, J., Lada, C.J., & Lada, E.A. 1999, ApJ, 515, 265

Bachiller, R. & Cernicharo, J. 1986, A&A, 168, 262

Ballesteros–Paredes, J., Hartmann, L., & Vázquez–Semadeni, E. 1999, ApJ, 527, 285

Bally, J. & Langer, W.D. 1982, ApJ, 255, 143

Beichman, C.A., Myers, P.C., Emerson, J.P., Harris, S., Mathieu, R., Benson, P.J., & Jennings, R.E. 1986, ApJ, 307, 377

Bertoldi, F. & McKee, C.F. 1990, ApJ, 354, 529

Burgh, E.B., France, K., & McCandliss, S.R. 2007, ApJ, 658, 446

Burton, W.B. & Hartmann, D. 1994, in Unveiling Large–Scale Structures Behind the Milky Way, ASP Conf. Series, Vol. 67, C. Balkowski & R.C. Kraan-Kortweg eds. (San Francisco: Astronomical Society of the Pacific), 31

Cernicharo, J., & Guélin, M. 1987, A&A, 176, 299

Chu, W.–H. & Watson, W.D. 1983, ApJ, 267, 151

Crutcher, R. M., & Troland, T.H. 2000, ApJ, 537, L139

Dickman, R.L., Snell, R.L., & Schloerb, F.P. 1986, ApJ, 309, 326

Duvert, G., Cernicharo, J., & Baudry, A. 1986, A&A, 164, 349

Elias, J.H. 1978, ApJ, 224, 857

Erickson, N.R., Grosslein, R.M., Erickson, R.B., & Weinreb, S. 1999, IEEE Trans. Microwave Theory Tech., 47(12), 2212

Federman, S.R., Strom, C.J., Lambert, D.L., Cardelli, J.A., Smith, V.V., & Joseph, C.L. 1994, ApJ, 424, 772

Frerking, M.A., Langer, W.D., & Wilson, R.W. 1982, ApJ, 262, 590

Goldsmith, P.F., Langer, W.D., Carlson, R.E., & Wilson, R.W. 1980, in Interstellar Molecules, IAU Symp. 87, B.H. Andrew ed. (Dordrecht: Reidel), 417

Goldsmith, P.F., Young, J.S., & Langer, W.D. 1983, ApJS, 51, 203

Goldsmith, P.F. & Li, D. 2005, ApJ, 622, 938

Gomez de Castro, A.I. & Pudritz, R.E. 1992, ApJ, 395, 501

Goodman, A.A., Jones, J.T., Lada, E.A., & Myers, P.C. 1992, ApJ, 399, 108

Hartigan, P., & Kenyon, S.J. 2003, ApJ, 583, 334

Hartmann, L., Ballesteros–Paredes, J., & Bergin, E. A. 2001, ApJ,562, 852

Hartmann, L. 2002, ApJ, 578, 914

Heiles, C. 2000, AJ, 119, 923

Heiles, C. & Crutcher, R. 2005, in Cosmic Magnetic Fields, R. Wielebinski & R. Beck ed. (Berlin: Springer), 137

Heyer, M.H., Vrba, F.J., Snell, R.L., Schloerb, F.P., Strom, S.E., Goldsmith, P.F., & Strom, K.M. 1987, ApJ, 321, 855

Heyer, M.H. 1988, ApJ, 324, 311

Jijina, J., Myers, P.C., & Adams, F.C. 1999, ApJS, 125, 161

Kainulainen, J., Lehtinen, K., & Harju, J. 2006, A&A, 447, 597

Kenyon, S. 2007, private communication; to appear in The Handbook of Star Forming Regions, ASP Conference Series, B. Reipurth, ed., 2008

Lacy, J.H., Knacke, R., Geballe, T.R., & Tokunaga, A.T. 1994, ApJ, 428, L69

Langer, W.D., Goldsmith, P.F., Carlson, E.R., & Wilson, R.W. 1980, ApJ, 235, L39

Langer, W.D., Wilson, R.W., Goldsmith, P.F., & Beichman, C.A. 1989, ApJ, 337, 355

Langer, W.D. & Penzias, A.A. 1993, ApJ, 408, 539

Langer, W.D., Velusamy, T., Kuiper, T.B.H., Levin, S., Olsen, E., & Migenes, V. 1995, ApJ, 453, 293

Li, D. & Goldsmith, P.F. 2003, ApJ, 585, 823

Li, D., Goldsmith, P.F., & Menten, K.M. 2003, ApJ, 587, 262

Liszt, H.S. & Lucas, R. 1998, A&A, 339, 561

Liszt, H.S. 2007, A&A, 476, 291

Mitchell, G.F., Sargent, A.I., & Mannings, V. 1997, ApJ, 483, L127

Mizuno, A., Onishi, T., Yonekura, Y., Nagahama, T., Ogawa, H., & Fukui, Y. 1995, ApJ, 445, L161

Moneti, A., Pipher, J.L., Helfer, H.L., McMillan, R.S., & Perry, M.L. 1984, ApJ, 282, 508

Narayanan, G., Heyer, M., Brunt, C., Snell, R.L., Goldsmith, P.F., & Li, D. 2007, submitted to ApJ

Onishi, T., Mizuno, A., Kawamura, A., Ogawa, H., & Fukui, Y. 1996, ApJ, 465, 815

Onishi, T., Mizuno, A., Kawamura, A., Ogawa, H., & Fukui, Y. 1998, ApJ, 502, 296

Onishi, T., Mizuno, A., Kawamura, A., Tachihara, K., & Fukui, Y. 2002, ApJ, 575, 950

Padoan, P., Cambrésy, L., & Langer, W.D. 1992, ApJ, 580, L57

Palla, F. & Stahler, S.W. 2000, ApJ, 540, 255

Palla, F. & Stahler, S.W. 2002, ApJ, 58, 1194

Palla, F. 2008, private communication

Pratap, P., Dickens, J.E., Snell, R. L., Miralles, M.P., Bergin, E.A., Irvine, W.M., & Schloerb, F.P. 1997, ApJ, 486, 862

Pringle, J.E., Allen, R.J., & Lubow, S.H. 2001, MNRAS, 327, 663

Schloerb, F.P., & Snell, R.L. 1984, ApJ, 283, 129

Shu, F.H., Adams, F.C., & Lizano, S. 1987, ARA&A, 25, 23

Shuter, W.L.H., Dickman, R.L., & Klatt, C. 1987, ApJ, 322, L103

Snell, R.L. 1981, ApJS, 45, 121

Sonnentrucker, P., Welty, D.E., Thorburn, J.A., & York, D.G. 2007, ApJS, 168, 58

Strong, A.W. & Mattox, J.R. 1996, A&A, 308, L21

Tamura, M., Gatley, I., Wall, W., & Werner, M.W. 1991, ApJ, 374, L25

Tatematsu, K., Umemoto, T., Kandori, R., & Sekimoto, Y. 2004, ApJ, 606, 333

Troland, T., Crutcher, R.M., Goodman, A.A., Heiles, C., Kazès, I., & Myers, P.C. 1996, ApJ, 471, 302

Ungerechts, H. & Thaddeus, P. 1987, ApJS, 63, 645

Van Dishoeck, E.F. & Black, J.H. 1988, ApJ, 334, 771

Vázquez–Semadeni, E. 2007, in Triggered Star Formation in a Turbulent ISM, Proc. IAU Symp. 237, B.G. Elmegreen & J. Palous, eds. (Cambridge: Cambridge University Press), 292

Watson, W.D., Anicich, V.G., & Huntress, W.T. Jr. 1976, ApJ, 205, L165

Young, J.S., Goldsmith, P.F., Langer, W.D., & Wilson, R.W. 1982, ApJ, 261, 513